JEM Journal of Experimental Medicine

ARTICLE

Functional targeting of ILC2s and ILC3s reveals selective roles in intestinal fibrosis and homeostasis

Ahmed Kabil[1], Natalia Nayyar[1], Chengxi Xu[1], Julyanne Brassard[1], Lesley A. Hill[2], Samuel B. Shin[1], Sameeksha Chopra[1], Bernard Lo[3], Yicong Li[1], Mya Bal[1], Marine Theret[1], Fabio M.V. Rossi[1,4], T. Michael Underhill[1,2], Michael R. Hughes[1], and Kelly M. McNagny[1,4,5]

Innate lymphoid cells (ILCs) are long-lived, tissue-resident cell analogs to T helper subsets that lack antigen-specific receptors. Understanding the roles of specific ILCs in chronic inflammation and fibrosis has been limited by inadequate tools for selective targeting. Here, we used *Il17rb-CreERT2-eGFP* and *Rorc-Cre* strains to selectively delete RORα in ILC2s and ILC3/Th17 cells, respectively. RORα deletion in ILC2s caused significant loss of gastrointestinal ILC2s, increased ILC3 abundance, elevated Th17-type responses, and heightened susceptibility to Crohn's disease–like fibrosis. Conversely, RORα deletion in ILC3/Th17 cells reduced IL-17 production, protecting against fibrosis. Using isolithocholic acid (isoLCA), a microbial secondary bile acid and RORγt inverse agonist, we confirmed the role of ILC3s/Th17 cells in fibrosis. In RORγt reporter and Th17-deficient *Rag1*$^{-/-}$ mice, isoLCA reduced IL-17 production by ILC3s and attenuated intestinal fibrosis by dampening RORγt-dependent ILC3/Th17 responses. These findings reveal a novel interplay between ILC2s and ILC3s in gut homeostasis and demonstrate the therapeutic potential of targeting RORγt in ILC3s as a strategy for preventing fibrosis.

Introduction

Innate lymphoid cells (ILCs) are tissue-resident immune-modulatory cells responsible for both mucosal tissue homeostasis and the early stages of host defense. The ILC family is classified into five major groups: natural killer (NK), ILC1, ILC2, ILC3, and lymphoid tissue inducer (LTi) cells, based on their developmental trajectories and functional characteristics (Vivier et al., 2018). NK cells primarily function as cytotoxic cells that circulate in the bloodstream and can be thought of as an innate branch of lymphocytes serving parallel functions to cytotoxic CD8$^+$ T cells. In contrast, ILC1, ILC2, and ILC3 subsets are functional analogs to the CD4$^+$ helper T cell subsets, Th1, Th2, and Th17, respectively (Eberl et al., 2015; Jan-Abu et al., 2023). While Th cells are exquisitely antigen-specific and take days to mature and activate in the lymph nodes, ILCs are tissue resident and respond rapidly to a variety of "alarmins" released locally at the site of tissue damage in an antigen-independent manner. These alarmins, elaborated by epithelial cells and stroma, play a crucial role in rapidly activating and polarizing innate immune responses within the affected tissues and include factors like thymic stromal lymphopoietin, interleukin (IL)-33, and IL-25 that selectively activate ILC2s, and IL-1β and IL-23 that activate ILC3s (Melo-Gonzalez and Hepworth, 2017). Thus, alarmins and ILCs resolve the age-old mystery of how the immune system has evolved to initiate rapid and appropriate helper responses tailored to pathogens before antigen-specific T cells are recruited and engaged.

Precisely how ILCs regulate mucosal barrier homeostasis has become a topic of intense interest since it is known that the dysregulation of ILC function is linked to a variety of chronic inflammatory diseases including asthma/atopy (Gold et al., 2014; Halim et al., 2014), psoriasis (Bielecki et al., 2021), inflammatory bowel disease (IBD) (Arifuzzaman et al., 2024; Buonocore et al., 2010), fibrosis (Lo et al., 2016), and cancer (Jacquelot et al., 2021; Jou et al., 2022; Schuijs et al., 2020). Nevertheless, due to their relatively recent discovery, a myriad of questions remains concerning ILC origins, plasticity, migratory behavior, and function (Kabil et al., 2022). This largely reflects a lack of adequate animal models and reporter assays to fate-map, lineage-trace, and genetically modify specific ILC subsets to directly address their origins and elucidate their physiological relevance in health and disease. While some such models have been developed (*Il7r*-Cre, *Id2*-CreERT2, *Arg1*-CreERT2, and *Rora*$^{sg/sg}$), these tend to either target all ILC subsets or influence other cell lineages dampening their utility for tracing or modifying individual ILC subsets (Cording et al., 2018). In an effort to address that gap, we report here the generation of an *Il17rb*-based transgenic (Tg) mouse line for selective ILC2 lineage tracing, fate mapping, and inducible deletion of targeted alleles. As a

[1]School of Biomedical Engineering, University of British Columbia, Vancouver, Canada; [2]Department of Cellular and Physiological Sciences, University of British Columbia, Vancouver, Canada; [3]Department of Pathology and Rogel Cancer Center, University of Michigan, Ann Arbor, MI, USA; [4]The Department of Medical Genetics, University of British Columbia, Vancouver, Canada; [5]The Center for Heart Lung Innovation, St Paul's Hospital, Vancouver, Canada.

Correspondence to Kelly M. McNagny: kelly@brc.ubc.ca; Michael R. Hughes: mhughes@brc.ubc.ca.

proof of concept, we show that selective deletion of the master transcription factor, RORα, effectively leads to striking reduction in gastrointestinal (GI) ILC2s. Conversely, to selectively address the function of ILC3s we used commercially available *Rorc-Cre* mice to delete RORα in ILC3s, rendering them defective in proliferation and IL-17 production.

Using these two novel strains, we investigate the role of ILC2 and ILC3 in a *Salmonella*-driven mouse model of Crohn's disease–like fibrosis (Grassl et al., 2008; Lo et al., 2016; Lo et al., 2019c). We find that deletion of RORα in gut ILC2s leads to a compensatory increase in the frequency of ILC3s and a dramatic increase in susceptibility to fibrosis. Conversely, we show that mice lacking functional ILC3s are potently protected from fibrosis. In both cases, these phenotypes are linked to the modulatory effects of RORα deletion on tissue IL-17 expression. Furthermore, we show in vitro that IL-17 activates purified gut fibroblasts to produce factors that further exacerbate IL-17–driven inflammation. Finally, we confirm these results pharmacologically using, isolithocholic acid (isoLCA), an abundant gut flora-derived metabolite that we find selectively inhibits RORγt activity in ILC3s and Th17 cells but has no effect on RORα activity in ILC2s and ILC3s. In summary, by selective genetic and pharmacological targeting of ILC2s and ILC3s we reveal their complex interplay in fibrotic disease and outline a rational approach to targeting these cells for therapy.

Results

Il17rb is a signature cytokine receptor gene uniformly expressed by tissue ILC2s

Analysis of single-cell transcriptomics of ILCs in the mouse gut at steady-state and under inflammatory conditions reveals that *Il17rb* expression is highly selective for ILC2s (Benoist et al., 2012; Gury-BenAri et al., 2016; Lo et al., 2019a) (Fig. S1, A–G). Accordingly, we modified this locus in murine embryonic stem (ES) cells to develop a new mouse model that labels all ILC2s at steady state while facilitating ILC2-specific gene deletion using a tamoxifen-inducible CreERT2 (*Il17rb-CreERT2-eGFP*, Fig. 1 A). Briefly, downstream of the *Il17rb* exon 11 we introduced a tamoxifen-inducible CreERT2 and an IRES-eGFP cassette resulting in a locus expressing polycistronic mRNAs that preserves the normal expression of the *Il17rb*-encoding transcript while permitting the ectopic expression of eGFP, and the co-expression of the tamoxifen-inducible CreERT2 enzyme (Fig. 1 A). Immunohistochemical and flow cytometry analyses of eGFP expression in the resultant mouse small intestine (SI) reveal *Il17rb*-regulated transgenes are expressed selectively within the hematopoietic compartment (Fig. 1 A and Fig. S1 H). Within the lamina propria, *Il17rb*-eGFP labels a discrete subpopulation of lineage-negative cells (non-T cell, non-B cell, non-myeloid cell: lineage markers: CD3e, CD3, CD5, CD8a, TCRb, CD11b, CD11c, CD19, B220, Ly6C, Ly6G, Ter119). Lineage$^-$*Il17rb*-eGFP$^+$ cells co-express CD127, IL-25R, KLRG1, and Sca-1 but lack the expression of CCR6, NKp46, and NK1.1, consistent with an ILC2 phenotype (Fig. 1, B and C). To validate that the endogenous *Il17rb* locus remains functional, we compared IL-25R expression (composed of IL17RA and IL17RB subunits), by ILC2s from wild-type (WT) and homozygous *Il17rb-CreERT2-eGFP* mice. The median fluorescence intensity (MFI) of IL-25R was similar between the two groups, confirming that the knock-in strategy did not affect endogenous *Il17rb* expression (Fig. S1 I).

Further examination of eGFP reporter expression shows that virtually all ILC2s transcribe the *Il17rb* locus across all major mucosal barrier sites of the body, including the lungs and skin (Fig. 1, D and E). It is noteworthy that although lung ILC2s are well known to lack expression of cell surface IL-25R (and the IL17RB subunit), these are robustly labeled by the eGFP knock-in construct, indicating that the transcript is expressed. Thus, the lack of cell surface IL17RB expression at the steady state likely reflects posttranscriptional regulation of the *Il17rb* mRNA. Enhanced GFP expression is also detected in all ILC2s in the lymph nodes and skeletal muscle, suggesting a versatile opportunity to monitor ILC2s in all tissues under various conditions. Importantly, using a variety of additional lineage markers (e.g., NKp46, NK1.1, CCR6), we find that *Il17rb* is not detectably expressed at the steady state in any of the other ILC sublineages (ILC1, ILC3, NK) or by adaptive immune cells, including CD4$^+$ T cells and CD8$^+$ T cells, in mucosal tissues (Fig. 1, F and G). Lastly, this immunophenotype precisely matches the *Il17rb* mRNA expression pattern of public single-cell RNA sequencing (scRNA-seq) data (Kiner et al., 2021) (Fig. S1, E and F).

With regard to precursors, we examined *Il17rb* expression in the thymus and bone marrow (BM). Thymic Lineage$^-$/CD127$^+$ cells constitutively express *Il17rb*-eGFP, and these cells also expressed high levels of CD25 and Sca-1 (Fig. S2, A and B). Investigating further we find low-level expression of *Il17rb-eGFP* in thymic CD1d$^+$ NKT cells and double-negative (DN) T cell precursors, which peaks on DN2 cells and drops off on DN3 and DN4 cells (Fig. S2, C–E). However, it should be noted that all Lineage$^-$*Il17rb-eGFP*$^+$ DN cells in the thymus exhibit seven- to eightfold lower levels of expression when compared to Lineage$^-$*Il17rb*$^+$ cells isolated from SI and Peyer's patches (Fig. S2 F).

In the adult BM, *Il17rb*-eGFP is expressed by a rare subset (0.13–0.16%) of CD45$^+$ cells. Notably, *Il17rb*-eGFP is absent in primitive hematopoietic stem and progenitor cells (HSPCs, defined as CD45$^+$Lineage$^-$Kit$^+$Sca-1$^+$) and in common lymphoid progenitors and common helper-like innate lymphoid progenitors (CD45$^+$Lineage$^-$Sca-1$^{-/int}$CD25$^-$). However, *Il17rb*-eGFP is readily detectable in Lineage$^-$CD127$^+$Sca-1$^+$CD25$^+$ cells, consistent with an ILC2 immunophenotype (Walker et al., 2015) (Fig. 1, H and I; and Fig. S3, A–C). By extending the SSC-A gating strategy, we further identified that 70–80% of eosinophil progenitors express eGFP (Fig. S3 D). However, these eosinophil progenitors exhibited lower *Il17rb* expression compared with ILC2s (Fig. S3 D). Collectively, these findings indicate that *Il17rb-CreERT2-eGFP* transcripts are most prominently expressed in ILC2s and a subset of committed eosinophil precursors within the BM.

Finally, to investigate potential changes in *Il17rb* expression within ILC2s and T cells under a strong type 2 inflammatory response, we administered IL-33 to adult mice via intranasal administration for three consecutive days and euthanized them 24 h after the last induction. We observed that *Il17rb* expression

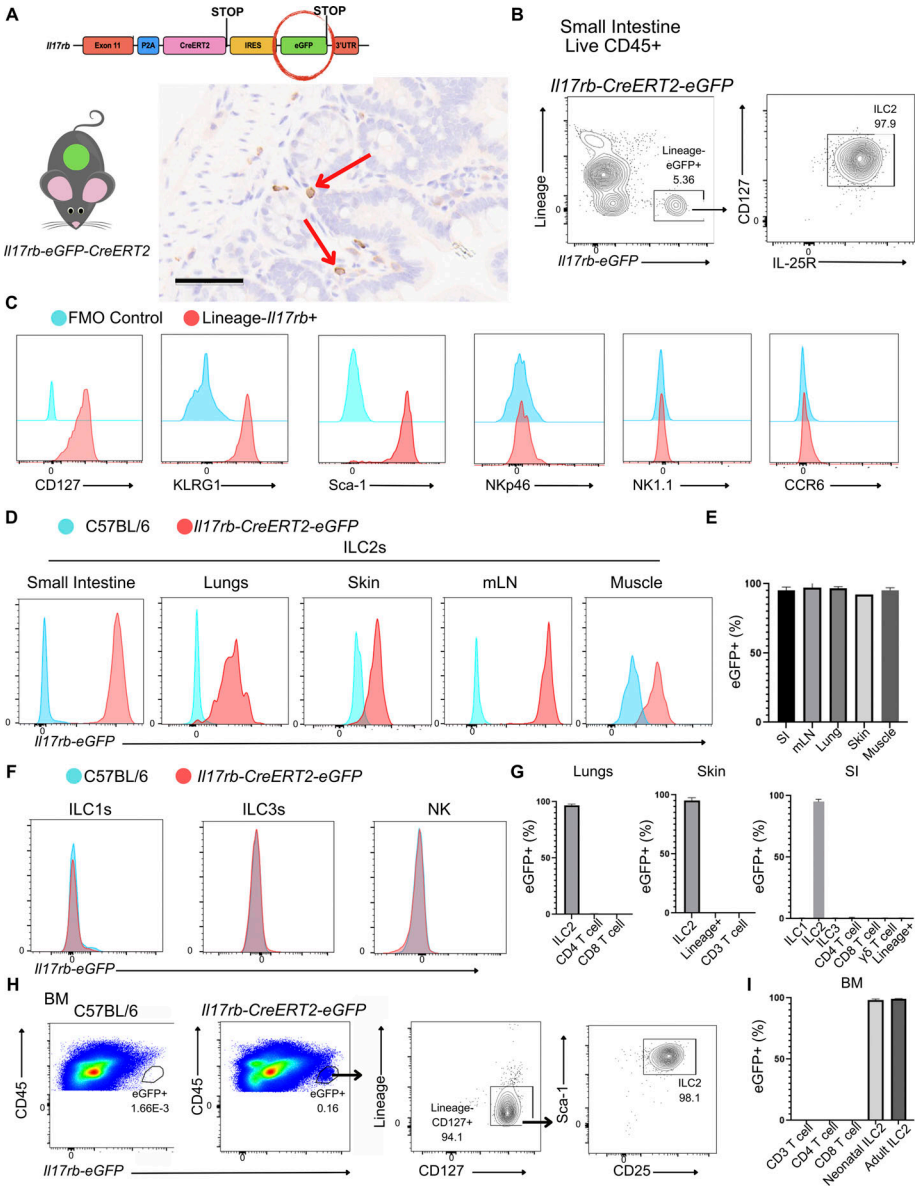

Figure 1. ***Il17rb-CreERT2-eGFP* Tg mice allow efficient lineage tracing of ILC2. (A)** Schematic representation of the genetic modification in *Il17rb-CreERT2-eGFP* mice, with a corresponding representative image of the SI showing eGFP-expressing cells (red arrows). Scale bar = 50 µm. **(B)** Representative flow cytometry plots demonstrating *Il17rb-eGFP*$^+$ expression by SI-LP cells. **(C)** Representative histograms displaying marker expression by *Il17rb-eGFP*$^+$ cells in the SI. **(D)** Histograms illustrating eGFP expression by ILC2s across various tissues. Small intestinal ILC2s were defined as Lineage$^-$CD127$^+$IL-25R$^+$KLRG1$^+$ cells. Lung ILC2s were defined as Lineage$^-$CD127$^+$ST2$^+$ cells. Skin ILC2s were defined as Lineage$^-$CD127$^+$CD103$^+$ cells. mLN ILC2s were defined as Lineage$^-$CD127$^+$IL-25R$^+$ cells. Muscle ILC2s were defined as Lineage$^-$CD127$^+$KLRG1$^+$ cells. **(E)** Quantification of *Il17rb-eGFP*$^+$ ILC2s in the SI, mLN, lungs, skin, and muscle (n = 3 mice). **(F)** Flow cytometry plots showing *Il17rb-eGFP*$^+$ expression in Lineage$^-$CD127$^+$NK1.1$^+$NKp46$^+$ ILC1s and Lineage$^-$CD127$^+$RORγt$^+$ ILC3s from Il17rb-CreERT2-eGFP mice. **(G)** Quantification of *Il17rb-eGFP*$^+$ cells within ILC1s, IL-25R$^+$KLRG1$^+$ ILC2s, ILC3s, CD4$^+$TCRβ$^+$ and CD8$^+$TCRβ$^+$ T cells, and CD45$^+$TCRγδ$^+$ cells relative to ILC2s in the lungs, skin, and SI (n = 3 mice). **(H)** Flow cytometry analysis of *Il17rb-eGFP*$^+$ cells in BM from naïve Il17rb-CreERT2-eGFP mice. **(I)** Quantification of *Il17rb-eGFP*$^+$ cells among adult and neonatal ILC2s compared with adaptive T cell lineages in the BM (n = 3 mice). Data from all panels are representative of three or more independent experiments. Data are means ± SEM. Lineage markers: CD3ε, CD3, CD5, CD8α, TCRβ, Cd11b, CD11c, CD19, B220, Ly6C, Ly6G, Ter119.

remained consistently high in IL-33–activated lung ILC2s, whereas expression in mature peripheral T cells remained negligible (Fig. S3, E–G). Enhanced GFP is also undetectable on eosinophils during IL-33–induced type 2 inflammation (Fig. S3 H). These findings further validate the eGFP portion of the *Il17rb-CreERT2-eGFP* construct as a specific and reliable marker of ILC2s at steady state and during the initial phase of type 2 inflammation in the periphery.

We also find that Lineage$^-$ cells in the fetal liver and intestine express *Il17rb*-eGFP, consistent with waves of committed ILC2 lineage cell seeding tissues and barriers early during development (Fig. 2, A and B). Consistent with previous studies, *Il17rb-*

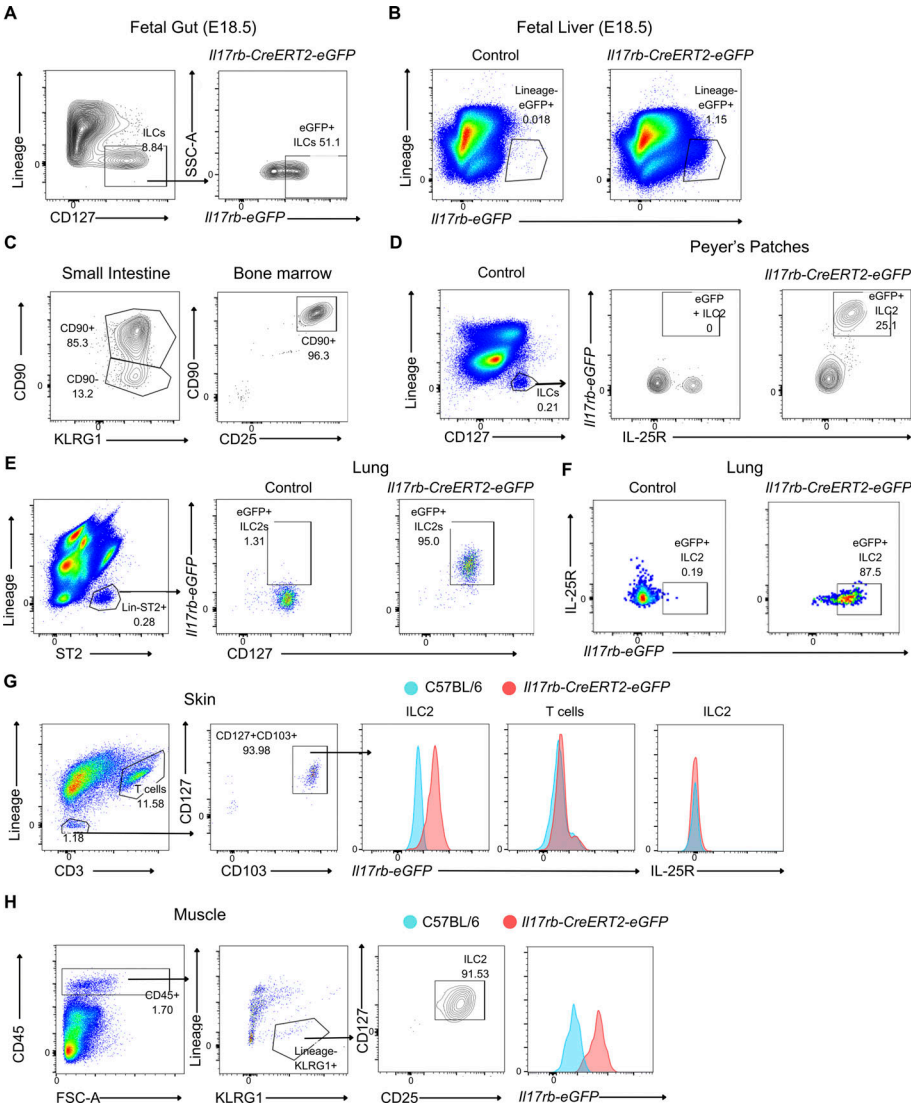

Figure 2. ***Il17rb*-eGFP marks all ILC2 irrespective of their distinct, tissue-specific coreceptor expression programs. (A)** Representative flow cytometry plots showing *Il17rb*-eGFP expression in ILCs from the fetal gut at E18.5. **(B)** Flow cytometry plots depicting *Il17rb*-eGFP expression in Lineage⁻ cells from the fetal gut. **(C)** Flow cytometry plots of live CD45⁺Lineage⁻*Il17rb*-eGFP⁺ cells in the SI and BM of 12-wk-old adult mice. **(D)** Representative flow cytometry plots of ILC2s in adult Peyer's patches. **(E and F)** Flow cytometry plots of ILC2s in the lungs of *Il17rb*-CreERT2-eGFP mice. **(G)** Flow cytometry plots of ILC2s in the adult skin, accompanied by representative histograms showing *Il17rb*-eGFP and IL-25R expression. **(H)** Flow cytometry plots of ILC2s in the muscle with a representative histogram of *Il17rb*-eGFP expression. Data from all panels are representative of three or more independent experiments.

eGFP-labeled ILC2s show tissue-specific heterogeneity in CD90 expression (Ricardo-Gonzalez et al., 2018; Schroeder et al., 2023): in BM, ILC2s are uniformly CD90⁺ ILC2s, whereas in small intestinal *Il17rb*-eGFP⁺, ILC2s are heterogeneous for CD90 expression (Fig. 2 C). *Il17rb*-eGFP⁺ ILC2s in Peyer's patches resemble small intestinal ILC2s and co-express CD127 and IL-25R (Fig. 2 D). Lung *Il17rb*-eGFP⁺ ILC2s express CD25 and ST2 but lack IL-25R expression, reflecting their selective responsiveness to IL-2 and IL-33, but not IL-25 (Fig. 2, E and F) (Martinez-Gonzalez et al., 2016; Steer et al., 2020). This suggests that *Il17rb* is transcribed but not translated. Skin *Il17rb*-eGFP⁺ ILC2s, which have been less well characterized, exhibit a standard ILC2 phenotype without IL-25R expression but with the co-expression of CD103 and CD127 (Fig. 2 G). In skeletal muscle, *Il17rb*-eGFP⁺ ILC2s express CD127 and KLRG1 at the steady state (Fig. 2 H). In summary, IRES-eGFP integration in the *Il17rb* gene's 3′-UTR enables robust tracking of ILC2s across tissues, aligning with known tissue-specific ILC2 profiles.

Fate mapping of IL-17Rb⁺ cells via *Il17rb*-CreERT2-eGFP mice crossed to an RFP reporter

To validate tamoxifen-inducible activation of the Cre recombinase in *Il17rb-CreERT2-eGFP* mice, we crossed them with *R26R-flox-STOP-flox RFP* reporter mice to fate-map all cells that express *Il17rb* at the time of tamoxifen administration. We observe highly efficient labeling of CD4⁻CD8⁻Lineage⁻eGFP⁺ cells (90–95%) within the small intestinal lamina propria (SI-LP) and Peyer's patches 10–14 days after tamoxifen treatment (Fig. 3, A and B). We also observe high RFP expression by BM ILC2s, suggesting that *Il17rb-CreERT2-eGFP* mice reliably fate-map and

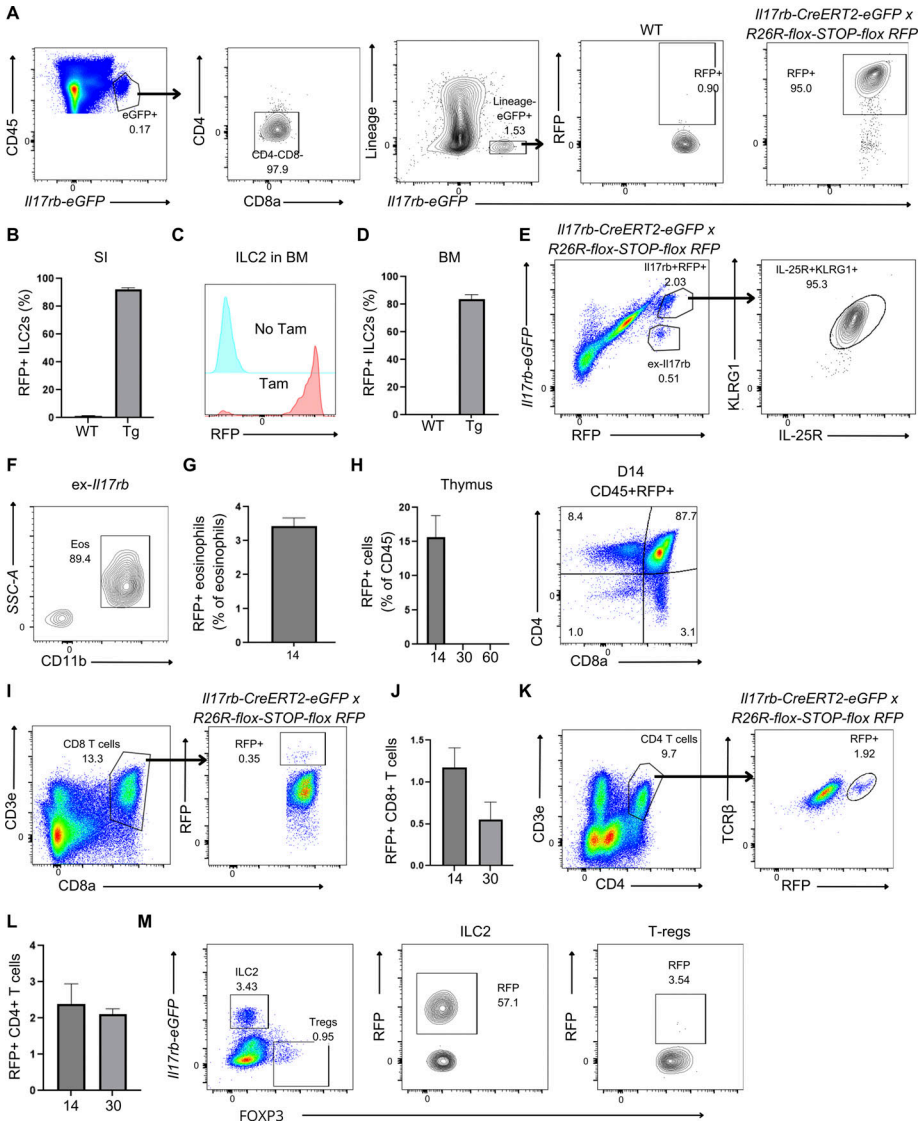

Figure 3. **Fate mapping of *Il17rb*⁺ cells via *Il17rb-CreERT2-eGFP* mice crossed to an RFP reporter. (A)** Representative flow cytometry plots showing Lineage⁻ Il17rb-eGFP⁺ (CD4⁻CD8⁻) cells in the SI-LP marked with RFP following tamoxifen administration. **(B)** Percentage of RFP⁺ ILC2s in the SI (n = 6 mice). **(C)** Representative histogram of RFP expression in BM ILC2s. **(D)** Percentage of RFP⁺ ILC2s in the BM following tamoxifen administration (n = 4 mice). **(E)** Representative flow cytometry plot showing *Il17rb*⁺RFP⁺ cells (IL-25R⁺KLRG1⁺ ILC2s) and ex-*Il17rb*⁺ cells in the SI 14 days after tamoxifen treatment. **(F)** Representative flow cytometry plot of ex-*Il17rb*⁺ cells, showing a SSC-A^{high}CD11b⁺ eosinophil phenotype. **(G)** Percentage of RFP⁺ eosinophils within CD64⁻CD11b⁺SSC-A^{high} eosinophils in the SI 14 days after tamoxifen treatment (n = 6 mice). **(H)** Quantification of RFP⁺ cells in the thymus and representative flow cytometry plots of RFP⁺ cells gated on CD4 and CD8 following five consecutive tamoxifen doses, with analysis at 14, 30, and 60 days after treatment (n = 3–5 mice). **(I)** Representative flow cytometry plots of CD8⁺ T cells in the SI and RFP expression. **(J)** Quantification of RFP⁺ cells within CD8⁺ T cells in the SI at 14 and 30 days after tamoxifen treatment (n = 6 mice). **(K)** Flow cytometry plots of CD4⁺ T cells in the SI and RFP expression. **(L)** Quantification of RFP⁺ CD4⁺ T cells in the SI at 14 and 30 days after tamoxifen treatment (n = 6 mice). **(M)** Representative flow cytometry plots comparing RFP expression in ILC2s versus Tregs in the SI 30 days after tamoxifen administration. WT refers to tamoxifen-treated *Il17rb-CreERT2-eGFP* mice, while Tg refers to tamoxifen-treated *Il17rb-CreERT2-eGFP* × *R26R-flox-STOP-flox RFP* mice. Data from all panels are representative of three or more independent experiments and are presented as the mean ± SEM.

track these cells across various tissues (Fig. 3, C and D). Thus, *Il17rb-CreERT2-eGFP* mice are an efficient tool for recombination of floxed alleles and modification of gene expression in the ILC2 lineage in vivo.

While all *Il17rb*⁺RFP⁺ cells were identified as KLRG1⁺IL-25R⁺ILC2s, we made a notable observation in the SI regarding a subset of "ex-*Il17rb*⁺" cells—cells that retained RFP expression but lacked *Il17rb*-eGFP (Fig. 3 E). Consistent with *Il17rb* expression on eosinophil progenitors, the majority of ex-*Il17rb*⁺ cells were SSC-A^{high}CD11b⁺ eosinophils (Fig. 3 F). However, given the short lifespan of eosinophils, we found that only 2–3% of the eosinophils remained fate-mapped 14 days after tamoxifen treatment, highlighting the transient nature of *Il17rb* expression within this lineage (Fig. 3 G). Importantly and consistent with our observation that *Il17rb*-eGFP⁺ is expressed at low levels of DN thymocytes, we find a substantial portion of

thymic DP and SP T cells are labeled by the RFP reporter immediately after our tamoxifen treatment regimen (up to 15%) (Fig. 3 H). However, these cells are virtually undetectable in thymus 30 days later and we find <2% of total peripheral tissue mature T cells are labeled (Fig. 3, I–L). In addition, FOXP3$^+$ regulatory T cells (Tregs) in the gut exhibited negligible RFP expression, whereas ILC2s retained robust labeling even 30–60 days after tamoxifen treatment (Fig. 3 M). These data suggest that when strongly induced with tamoxifen, *Il17rb-CreERT2-eGFP* mice may offer an additional exciting opportunity for pulse labeling T cell progenitors and monitoring thymic output over time (manuscript in preparation).

ILC2s regulate the homeostatic frequency of immune cell subsets in tissues

Previously, it was reported that the generation/specification of ILC2s is critically dependent on the expression of the master transcription factor, RORα (Halim et al., 2012). To explore this phenomenon more carefully, we crossed *Rora*$^{fl/fl}$ mice with *Il17rb*-eGFP-CreERT2 Tg mice, and induced *Rora* deletion via tamoxifen treatment (5 consecutive days) followed by a 7–14-day washout period. While this regimen has no effect on the frequency of peripheral T cells or any other immune cell subsets, deletion of RORα results in a threefold reduction in the absolute number of SI ILC2 and more than a twofold reduction in their frequency among the total SI CD45$^+$ cells including those ILC2s producing intracellular IL-4 and IL-13 (Fig. 4, A–E). These residual ILC2s also exhibit a significant reduction in the levels of cell surface IL-25R expression (Fig. 4 F). These elements aside, it is noteworthy that a subset of functional ILC2s persists following RORα inactivation. To determine whether this persistence resulted from inefficient targeting of the *Rora* locus in some ILC2s or whether distinct ILC2 subsets exhibit differential dependency on RORα, we sorted residual ILC2s (CD45$^+$Lineage$^-$*Il17rb*$^+$IL-25R$^+$KLRG1$^+$RFP$^+$) from the SI of *Il17rb-CreERT2-eGFP* × *R26-RFP* × *Rora*$^{fl/fl}$ mice and performed genomic PCR to amplify *Rora* exons 3 and 4 (Fig. 4, G and H). Surprisingly, we find that these residual SI ILC2s exhibit effective deletion of exon 4 (KO), whereas WT ILC2s retained full-length *Rora* transcripts (Fig. 4 H). These findings indicate that while a major subset of adult ILC2s is dependent on RORα for survival, another subset persists even in its absence, highlighting a previously unappreciated heterogeneity within the ILC2 compartment.

To examine the effects of long-term *Rora* deletion, neonates (P11-P13) were treated with three consecutive daily doses of tamoxifen and the ILC2 pool was subsequently analyzed 4 wk later (6 wk old). Using this approach, we observe a fivefold reduction in the absolute number of IL-25R$^+$ ILC2s and a fourfold decrease in GATA3$^+$ *Il17rb*$^+$ ILC2s, confirming that the early-life depletion of ILC2s leads to a lasting reduction in these populations (Fig. S4, A–C). This decline is, again, accompanied by the decreased expression of the canonical SI ILC2 marker, IL-25R. (Fig. S4 D).

Although the frequency of ILC2s in tamoxifen-treated *Il17rb-CreERT2-eGFP* × *R26-RFP* × *Rora*$^{fl/fl}$ mice is greatly reduced, we find that this residual ILC2 subset is enriched for cells producing IL-5 and IL-13 when compared to littermate controls (Fig. S4, E–G). Recent reports have also noted the presence of atypical IL-10–producing ILC2s in the gut (Bando et al., 2020), but their functional significance remains obscure. We find that depletion of RORα in adult ILC2s is accompanied by a nearly twofold reduction in the frequency of IL-10$^+$ ILC2 and, correspondingly, a threefold reduction in total cecal IL-10 (*Il10*) transcripts (Fig. 4, I–L).

As an anti-inflammatory cytokine, IL-10 has been shown to inhibit Th1 and Th17 cell function, possibly to ensure that effector T cell responses do not become hyperresponsive resulting in immunopathology (Glocker et al., 2009; Saraiva and O'Garra, 2010). In addition, IL-10 has potent suppressive affects by downregulating MHCII expression and antigen presentation by professional antigen-presenting cells (APCs) (Guo, 2016). Consistent with attenuation of these IL-10–driven functions, we observe a threefold increase in Th17 cells in the gut of tamoxifen-treated *Rora*^{iIL17Rb} mice (Fig. 4, M and N). We also observe a twofold increase in interferon gamma (IFNγ) production from CD4$^+$ Th1 cells in the SI-LP (Fig. 4, O–Q). Corresponding to reduced IL-10 and the role of IFNγ in stimulating macrophage activation (Murray and Wynn, 2011), ILC2-depleted *Rora*^{iIL17Rb} mice also exhibited an increased number of MHCII$^+$CD64$^+$-activated macrophages in the SI-LP, along with elevated levels of MHCII expressed on macrophages (Fig. 4, R–T).

Finally, we also observe a threefold expansion of gut ILC3s, the major granulocyte–macrophage colony-stimulating factor (GM-CSF) producing immune subset in the SI (Mortha et al., 2014), in *Rora*^{iIL17Rb} mice (Fig. 4 U). Previously, we showed that these cells are primary drivers of gut fibrosis in a Crohn's disease model (Lo et al., 2016), but despite this expansion, Masson's trichrome staining of cecal tissue revealed no significant differences in collagen deposition or histological signs of IBD at steady state (Fig. S4 H). In summary, while these findings suggest that ILC2s regulate the homeostatic balance of gut immune cell subsets at steady state and that this balance is perturbed in their absence, we find no evidence of overt pathology under baseline conditions.

Intestinal ILC2s constrain IL-17A–producing ILC3 during inflammation and fibrosis

Previously, we showed that pan-hematopoietic deletion of RORα protects mice from tissue fibrosis in a murine model of Crohn's disease (Lo et al., 2016; Lo et al., 2019a). Intriguingly, these and other studies showed that in addition to playing a critical role in development of ILC2s, RORα also plays an underappreciated role in regulating ILC3 and Th17 cell effector functions. Specifically, RORα was shown to be a key regulator of IL-17 production by ILC3 and Th17 cells (Eberl and Littman, 2004; Eberl et al., 2004; Gold et al., 2014; Halim et al., 2014; Hall et al., 2022; Lo et al., 2016; Lo et al., 2019a; Yang et al., 2008). Accordingly, the new *Rora*^{iIL17Rb} strain offers an opportunity to now directly assess the selective roles of ILC2s and ILC3s in Crohn's-type fibrosis. To test this, we infected *Rora*^{iIL17Rb} mice with an attenuated strain of *Salmonella* (Δ*aroA*), which leads to a transient local intestinal infection and inflammation, followed by the development of durable transmural GI fibrosis highly reminiscent of severe Crohn's disease (Fig. 5 A) (Ehrhardt et al., 2019; Lo et al., 2019c).

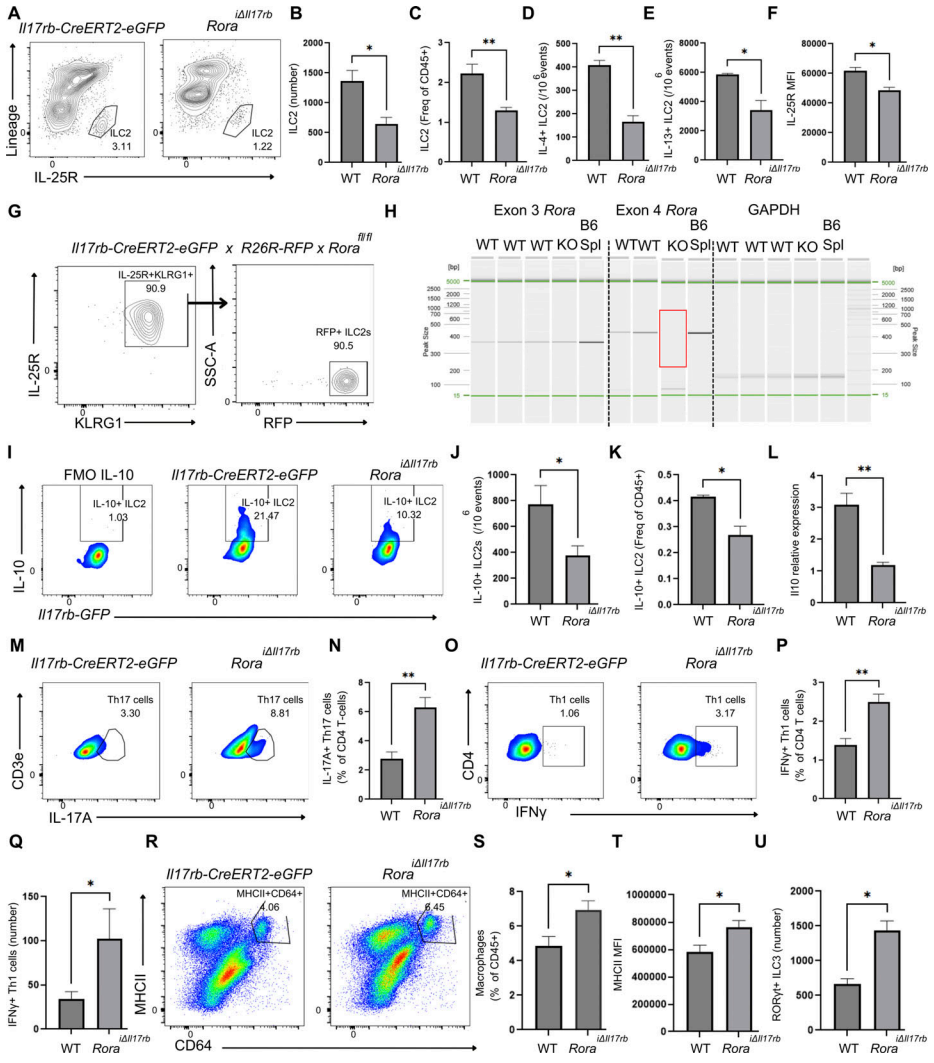

Figure 4. **ILC2s regulate the homeostatic frequency of immune cell subsets in tissues. (A)** Representative flow cytometry plots of live CD45⁺Lineage⁻IL-25R⁺ ILC2s in the SI after tamoxifen treatment (5 consecutive days) followed by a 7–14-day washout period. **(B and C)** Quantification of total ILC2 numbers and frequency (n = 3–4 mice). **(D and E)** Quantification of live CD45⁺Lineage⁻CD3⁻*Il17rb*⁺IL-4⁺ and IL-13⁺ ILC2s (n = 3 mice per group). **(F)** IL-25R expression levels in ILC2s (n = 3 mice). **(G)** Gating strategy for sorting ILC2s from the SI of *Il17rb*-CreERT2-eGFP × R26-RFP × *Rora*$^{fl/fl}$ mice (n = 2–3 mice pooled per experiment). **(H)** Genomic PCR analysis of *Rora* exon 3 and 4 rearrangement in small intestinal ILC2s. *Gapdh* was used as a loading control, and splenocytes from C57BL/6J mice served as a reference. **(I)** Representative flow cytometry plots of IL-10 expression in Lineage⁻IL-13⁺ ILC2s from the SI. **(J and K)** Quantification of Lineage⁻IL-13⁺IL-10⁺ ILC2s and frequency of IL-10⁺ ILC2s (n = 3 mice). **(L)** *Il10* transcript levels in the cecum (n = 3–4 mice). **(M)** Representative flow cytometry plots of IL-17A production by CD4⁺ Th17 cells. **(N)** Frequency of IL-17A⁺ Th17 cells in the SI (n = 5–7 mice). **(O)** Representative flow cytometry plots of IFNγ production by CD4⁺ Th1 cells. **(P and Q)** Frequency and quantification of IFNγ⁺ Th1 cells in the SI (n = 4–7 and n = 3 mice, respectively). **(R)** Representative flow cytometry plots of MHCII⁺CD64⁺ macrophages in the SI. **(S)** Frequency of macrophages (n = 3 mice). **(T)** MHCII expression levels in MHCII⁺CD64⁺ macrophages (n = 3 mice). **(U)** Quantification of Lineage⁻RORγt⁺ ILC3s (n = 3 mice). WT mice refer to *Il17rb-CreERT2-eGFP* mice (both groups were tamoxifen-treated at the same time). Data are representative of two to three independent experiments. Data are presented as the mean ± SEM. Statistical significance was determined using an unpaired two-tailed t test. *P < 0.05, **P < 0.01; ns, not significant. Lineage markers: CD3ε, CD3, CD5, CD8α, TCRβ, Cd11b, CD11c, CD19, B220, Ly6C, Ly6G, Ter119. For the detection of intracellular cytokines, isolated cells were stimulated with 50 ng/ml PMA (Sigma-Aldrich) and 750 ng/ml ionomycin (Sigma-Aldrich) for 4–6 h in the presence of 10 µg/ml brefeldin A (Sigma-Aldrich) in complete RPMI-1640 medium (containing 10% FBS, 50 mM 2-mercaptoethanol, 1 mM L-glutamine, 100 U/ml penicillin, and 100 µg/ml streptomycin) to evaluate their cytokine production. PMA, phorbol 12-myristate 13-acetate. Source data are available for this figure: SourceData F4.

We find that tamoxifen-mediated deletion of RORα in ILC2s leads to a twofold decrease in their frequency and a threefold reduction in their numbers in *Salmonella*-infected mice (Fig. 5, A–D). Although both WT and ILC2-deficient *Rora*^{iIL17Rb} mice exhibit equal susceptibility to colonization with *Salmonella* and an equivalent ability to clear this infection over time (Fig. 5 E), we observe a threefold expansion of Lineage⁻RORγt⁺ ILC3 in the SI-LP in the ILC2-deficient mice along with a higher frequency of IL-17A+ ILC3s in the SI and mesenteric lymph node (mLN) (Fig. 5, F–I). Likewise, depletion of ILC2 in mLN results in a similar shift toward increased type 3 immune responses as evidenced by a fourfold increase in RORγt⁺ ILC3s and two- to threefold increase in IL-17A⁺ ILC3s in the mLNs of *Rora*^{iIL17Rb} mice (Fig. 5, J–L). In addition, we find that depletion of SI ILC2s

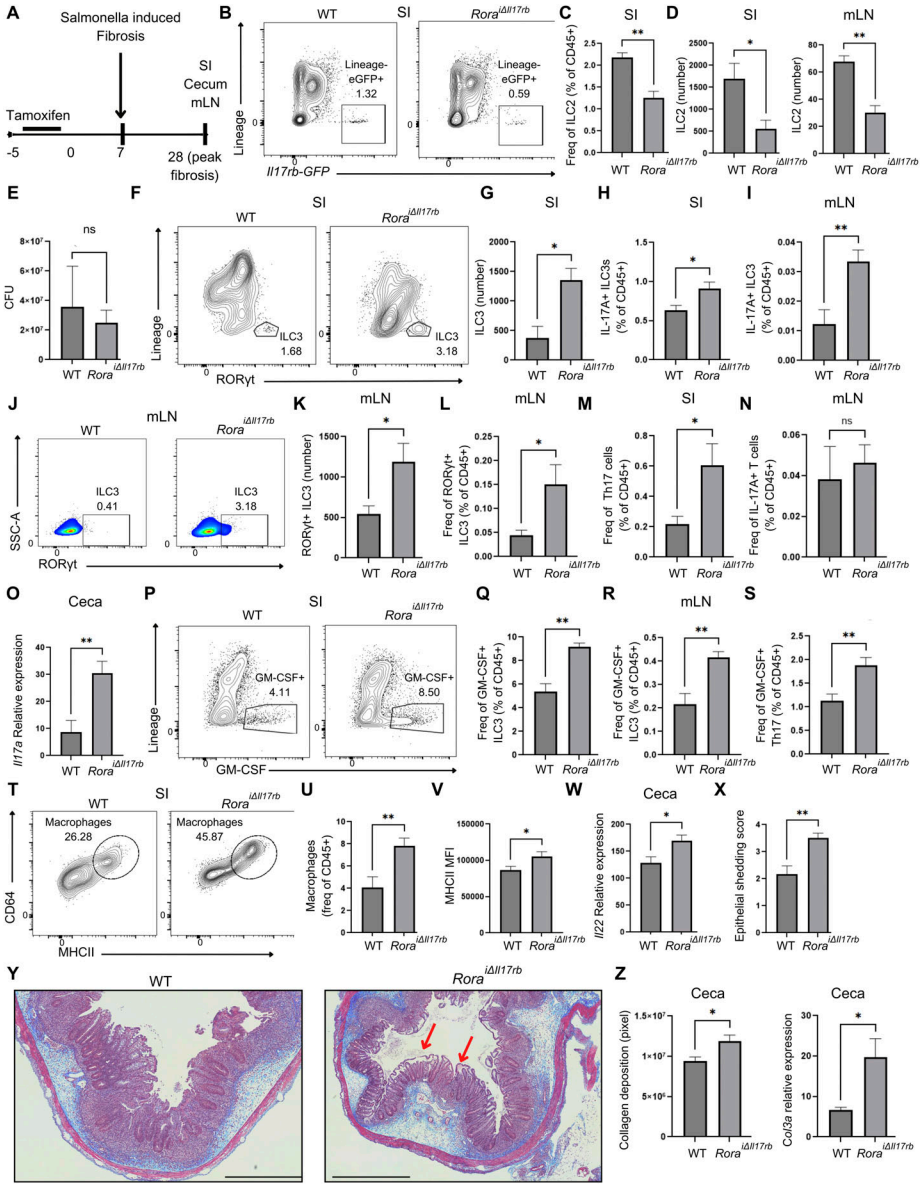

Figure 5. **Intestinal ILC2s constrain type 3 immune response during fibrosis. (A)** Experimental schematic depicting tamoxifen administration and analysis timeline. **(B)** Representative flow cytometry plots showing live CD45⁺Lineage⁻*Il17rb*-eGFP⁺ ILC2s in the SI of *Salmonella*-infected mice. **(C)** Frequency of ILC2s in the SI (n = 3–4 mice). **(D)** Absolute number of ILC2s in the SI and mLNs (n = 3–5 mice). **(E)** CFU counts of *Salmonella* isolated from the cecum (n = 5–7 mice). **(F)** Representative flow cytometry plots of live CD45⁺Lineage⁻RORγt⁺ ILC3s. **(G)** Absolute number of ILC3s in the SI (n = 3–4 mice). **(H)** Frequency of IL-17A⁺ live CD45⁺Lineage⁻RORγt⁺ ILC3s in the SI (n = 4–5 mice). **(I)** Frequency of IL-17A⁺CD45⁺Lineage⁻RORγt⁺ ILC3s in the mLN (n = 4–5 mice). **(J)** Flow cytometry plots showing live CD45⁺Lineage⁻RORγt⁺ ILC3s in the mLN. **(K)** Absolute number of ILC3s in the mLN (n = 5–6 mice). **(L)** Frequency of Lineage⁻RORγt⁺ ILC3s in the mLN (n = 5–6 mice). **(M)** Frequency of Lineage⁺CD3⁺IL-17A⁺ Th17 cells in the SI (n = 5–7 mice). **(N)** Frequency of Lineage⁺CD3⁺IL-17A⁺ Th17 cells in the mLN (n = 4–5 mice). **(O)** *Il17a* relative transcript levels in the cecum (n = 5–6 mice). **(P)** Flow cytometry plots showing live CD45⁺Lineage⁻GM-CSF⁺ ILC3s in the SI. **(Q)** Frequency of GM-CSF⁺ ILC3s in the SI (n = 4–6 mice). **(R)** Frequency of GM-CSF⁺ ILC3s in the mLN (n = 4–5 mice). **(S)** Frequency of GM-CSF⁺ Lineage⁺CD3⁺ Th17 cells in the SI (n = 4–5 mice). **(T)** Representative flow cytometry plots of CD64⁺MHCII⁺ macrophages in the SI. **(U)** Frequency of macrophages in the SI (n = 4–5 mice). **(V)** MHCII expression levels on macrophages in the SI (n = 4–5 mice). **(W)** *Il22* relative transcript levels in the cecum (n = 5 mice). **(X)** Quantification of epithelial shedding score (n = 5–7 mice). **(Y)** Representative Masson's trichrome–stained cecal tissue sections. Scale bar = 1,000 µm. **(Z)** Quantification of collagen deposition and *Col3a* transcript levels (n = 4 mice). Data are representative of two to three independent experiments. *Rora*^{iIL17Rb} refers to *Il17rb*-CreERT2-eGFP × *Rora*$^{fl/fl}$ mice. WT mice refer to *Il17rb-CreERT2-eGFP* mice (both groups were tamoxifen-treated at the same time). Data are presented as the mean ± SEM. Statistical significance was determined using an unpaired two-tailed t test. *P < 0.05, **P < 0.01; ns, not significant. Lineage markers: CD3ε, CD3, CD5, CD8α, TCRβ, Cd11b, CD11c, CD19, B220, Ly6C, Ly6G, Ter119. For the detection of intracellular cytokines, isolated cells were stimulated with 50 ng/ml PMA (Sigma-Aldrich) and 750 ng/ml ionomycin (Sigma-Aldrich) for 4–6 h in the presence of 10 µg/ml brefeldin A (Sigma-Aldrich) in complete RPMI-1640 medium (containing 10% FBS, 50 mM 2-mercaptoethanol, 1 mM *L*-glutamine, 100 U/ml penicillin, and 100 µg/ml streptomycin) to evaluate their cytokine production. PMA, phorbol 12-myristate 13-acetate.

also leads to increased Th17 cells in the SI, but not a significant difference in mLNs (Fig. 5, M and N). Collectively, these observations are consistent with the threefold increase in IL-17A (*Il17a*) gene expression we observe in *Salmonella*-infected $Rora^{iIL17Rb}$ mice compared with control mice (Fig. 5 O).

SI ILC3s are known to be the primary source of GM-CSF in the gut (Mortha et al., 2014), and consistent with the expanded ILC3 population in $Rora^{iIL17Rb}$ mice, we find increased GM-CSF production by ILCs in the SI and mLN of these mice compared with infected littermate controls (Fig. 5, P–R). Th17 cells can also produce GM-CSF in the inflamed intestine (Griseri et al., 2012; Mortha et al., 2014), and we found Th17 cells produced more GM-CSF in *Salmonella*-infected $Rora^{iIL17Rb}$ mice, compared with infected littermate controls (Fig. 5 S). However, we find that ILC3s are much more dominant producers of GM-CSF as evidenced by the fourfold difference in production by ILC3s versus Th17 cells in $Rora^{iIL17Rb}$-infected mice (Fig. 5 P). GM-CSF is well known for its ability to induce myeloid lineage differentiation and promote the survival of tissue mononuclear phagocytes (Castro-Dopico et al., 2020). In this regard, we also observe a 2.5-fold elevation in activated macrophages with increased MHCII expression in $Rora^{iIL17Rb}$ mice with active *Salmonella* infection (Fig. 5, T–V).

Consistent with more ILC3 in the SI and mLN, we also observe higher levels of IL-22 (*Il22*) transcripts in the ceca of $Rora^{iIL17Rb}$ mice (Fig. 5 W). IL-22 is known to be a key stabilizer of epithelial cell junctions and to maintain epithelial barrier integrity during infection and inflammation (Lo et al., 2019b). Interestingly, despite the excess fibrotic matrix deposition driven by increased secretion of IL-17A in $Rora^{iIL17Rb}$ mice and the significantly higher levels of the expression of collagen type 3 alpha gene, a key biomarker of fibrosis, we also observe evidence of atypical luminal shedding of intact epithelial linings in these mice (Fig. 5, X–Z). This would be consistent with a the role of IL-22 in preserving junctions between neighboring epithelial cells, even in the face of subepithelial inflammation and matrix deposition (Lo et al., 2019b). Taken together, these data underscore a critical and underappreciated role of ILC2 in restraining ILC3 numbers and type 3 immune responses in the gut, particularly during intestinal fibrotic responses.

Crohn's disease–like intestinal fibrosis is IL-17A dependent

Enhanced ILC3 numbers and functional activity in ILC2-deficient mice lead to exacerbated intestinal fibrosis, highlighting ILC3s as key drivers of the fibrotic response. Previously, we and others showed that RORα is not only critical for ILC2 development but also serves an additional role in regulating ILC3 and Th17 cell effector functions, likely through transcriptional upregulation of the ILC3 and Th17 lineage–specific genes, and directly regulating RORγt expression levels (Eberl and Littman, 2004; Eberl et al., 2004; Gold et al., 2014; Halim et al., 2014; Hall et al., 2022; Lo et al., 2019a; Lo et al., 2016; Yang et al., 2008). To further explore the selective role of ILC2 and ILC3/Th17 cells in fibrosis, we crossed *Rorc*-Cre to *Rora*-"floxed" mice to create a $Rora^{\Delta Rorc}$ strain that selectively lacks *Rora* in ILC3 and Th17 cells. Effectively, this creates mice with defective ILC3 and Th17 cells while sparing *Rora*-dependent ILC2 and other *Rora*-expressing cell types (Fig. 6 A) (Eberl and Littman, 2004; Eberl et al., 2004; Gold et al., 2014; Halim et al., 2014; Hall et al., 2022; Lo et al., 2016; Lo et al., 2019a; Yang et al., 2008).

To evaluate the functional responsiveness of *Rora*-deficient ILC3, we harvested lymphocytes from mLN and Peyer's patches of *WT* and $Rora^{\Delta Rorc}$ mice and stimulated them ex vivo with PMA, ionomycin, and brefeldin A plus IL-1β, as a proinflammatory cytokine known to activate ILC3 in various contexts (Mortha et al., 2014). While this treatment elicits robust IL-17A production from *WT* gut lymphocytes, $Rora^{\Delta Rorc}$ gut lymphocytes exhibit fivefold fewer RORγt$^+$IL-17A$^+$ cells after stimulation indicating a diminished ability to expand and produce type 3 immune signature cytokines (Fig. 6 B). This aligns with our previous scRNA-seq analyses of purified ILC3s from $Rora^{sg/sg}$ mice, which revealed a reduced expression of cytokine receptors, including the IL-1β receptor in the absence of RORα (Lo et al., 2019a). Furthermore, RORγt$^+$ ILC3s displayed markedly reduced RORγt expression levels (Fig. S5 A). This is consistent with our earlier scRNA-seq studies demonstrating diminished *Rorc* gene expression in RORα-deficient ($Rora^{sg/sg}$) chimeric mice (Lo et al., 2019a). Thus, loss of RORα in ILC3s diminishes their ability to respond to environmental cues, thereby rendering them dysfunctional and with a reduced capacity to secrete IL-17A.

Consistent with a recent report in which ILC3/Th17-deficient mice in the intestine were used to study ILC3 function, depletion of ILC3s/Th17 cells had no effect on the number of ILC2s (Araujo et al., 2024) (Fig. S5, B and C). To gain more insights into how RORα alters ILC3 homeostasis, we reanalyzed our previous scRNA-seq dataset of purified ILCs from $Rora^{sg/sg}$ mice and reclustered the ILC3 subset (Fig. S5 D). As expected, three major ILC3 populations emerged: NKp46$^+$ (T-bet$^+$) ILC3s, LTi-like ILC3s, and DN ILC3s. Notably, $Rora^{sg/sg}$ mice exhibited altered ILC3 subset frequencies, with a significant reduction in NKp46$^+$ ILC3s, while the frequency of LTi-like ILC3s remained largely unchanged (Fig. S5, E and F). Together, these findings demonstrate that RORα regulates RORγt expression across all ILC3 subsets and highlights NKp46$^+$ (T-bet$^+$) ILC3s as particularly sensitive to RORα inactivation. This suggests that RORα is essential for the survival of NKp46$^+$ ILC3s but not LTi-like ILC3s, and aligns well with a recent report indicating that NKp46$^+$ ILC3s are more sensitive to transcription factor perturbation (Fiancette et al., 2021).

To address whether deletion of RORα in RORγt$^+$ lineages alters disease responses in persistent intestinal inflammation, we infected $Rora^{\Delta Rorc}$ mice and control littermates with attenuated *Salmonella* (Fig. 6 C). At day 21 after *Salmonella* infection, we found threefold fewer ILC3 in $Rora^{\Delta Rorc}$ mLN, compared with infected *WT* littermates, as well as a threefold reduction in the frequency of RORγt$^+$ Th17 cells (Fig. 6, D–F). Thus, subsets of both innate and adaptive arms of the type 3 response are severely attenuated in $Rora^{\Delta Rorc}$ mice.

Gene expression analysis of ceca in *Salmonella*-infected $Rora^{\Delta Rorc}$ mice also revealed a dramatic decrease (approximately fourfold) in the expression levels of IL-17A transcript (*Il17a*)

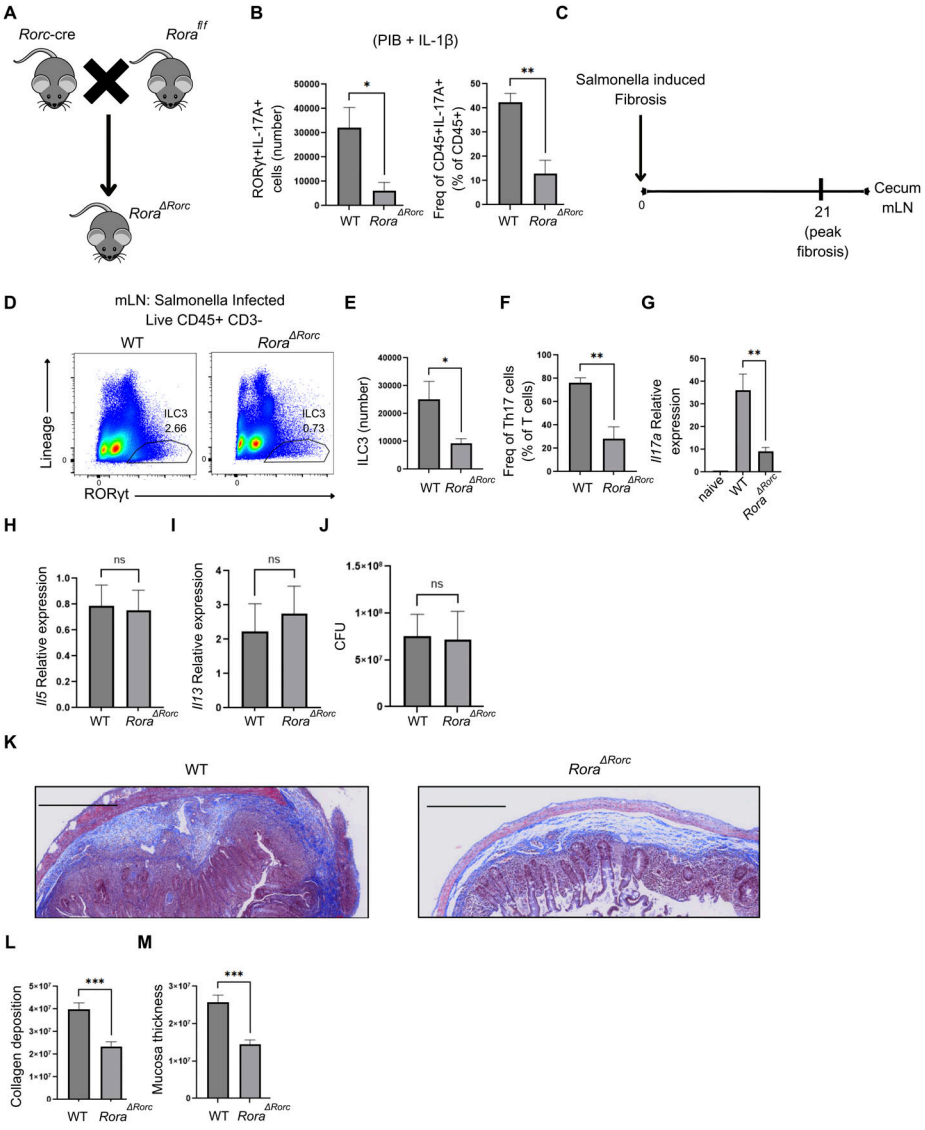

Figure 6. **Crohn's disease–like intestinal fibrosis is IL-17A dependent. (A)** Schematic representation of the generation of *Rora*$^{\Delta Rorc}$ mice. **(B)** Absolute number and frequency of IL-17A$^+$RORγt$^+$ cells isolated from Peyer's patches (n = 3–4 mice). **(C)** Experimental schematic outlining the study design. **(D)** Representative flow cytometry plots showing live CD45$^+$Lineage$^-$CD3$^-$RORγt$^+$ ILC3s in the mLNs (n = 3–4 mice). **(E)** Absolute number of live CD45$^+$Lineage$^-$RORγt$^+$ ILC3s (n = 4–5 mice). **(F)** Frequency of Th17 cells within the CD4$^+$ T cell population (n = 4–5 mice). **(G)** *Il17a* transcript levels in the cecum (n = 7–8 mice). **(H)** *Il5* transcript levels in the cecum (n = 7–8 mice). **(I)** *Il13* transcript levels in the cecum (n = 7–8 mice). **(J)** CFU counts from cecal samples (n = 7–8 mice). **(K)** Representative Masson's trichrome–stained cecal tissue sections showing collagen deposition. Scale bar = 1,000 µm. **(L)** Quantification of collagen deposition in the cecum. **(M)** Measurement of mucosal thickness (n = 7–8 mice). WT mice refer to *Rora*$^{fl/fl}$ littermate controls. Lineage markers: CD3ε, CD3, CD5, CD8α, TCRβ, Cd11b, CD11c, CD19, B220, Ly6C, Ly6G, Ter119. Data are representative of two independent experiments and are presented as the mean ± SEM. Statistical significance was determined using an unpaired two-tailed t test (*P < 0.05, **P < 0.01, ***P < 0.001; ns, not significant).

(Fig. 6 G). In contrast, we observe no significant differences in the expression of transcripts for IL-5 (*Il5*) or IL-13 (*Il13*) in *Salmonella*-infected WT and *Rora*$^{\Delta Rorc}$ mice (Fig. 6, H and I). These data align with our previous observations that fibrosis in this model occurs independently of type 2 cytokines and instead is driven predominantly by IL-17 (Lo et al., 2016). Also, consistent with previous reports, we find that this failure to produce IL-17A is accompanied by attenuated fibrotic matrix deposition (greater than twofold) in the cecum and significantly less mucosal thickening despite a similar ability to clear the *Salmonella* infection (Fig. 6, J–M).

IL-17A–driven transcriptional reprogramming of cecal fibroblasts fuels feedforward Th17/ILC3 regulation

To further elucidate how IL-17A drives fibrosis and intestinal inflammation, we isolated fibroblasts from the cecum and cultured them with IL-17A (20 and 200 ng/ml) before performing bulk RNA sequencing (Fig. 7 A). Notably, IL-17A exposure induced the upregulation of genes critical for Th17 effector function. Among the top differentially expressed genes were *Il6* and *Saa3*, which together amplify Th17 differentiation and effector activity (Fig. 7 B) (Lee et al., 2020). Specifically, *Saa3* functions as a potent adjuvant that enhances the pathogenicity of Th17 cells

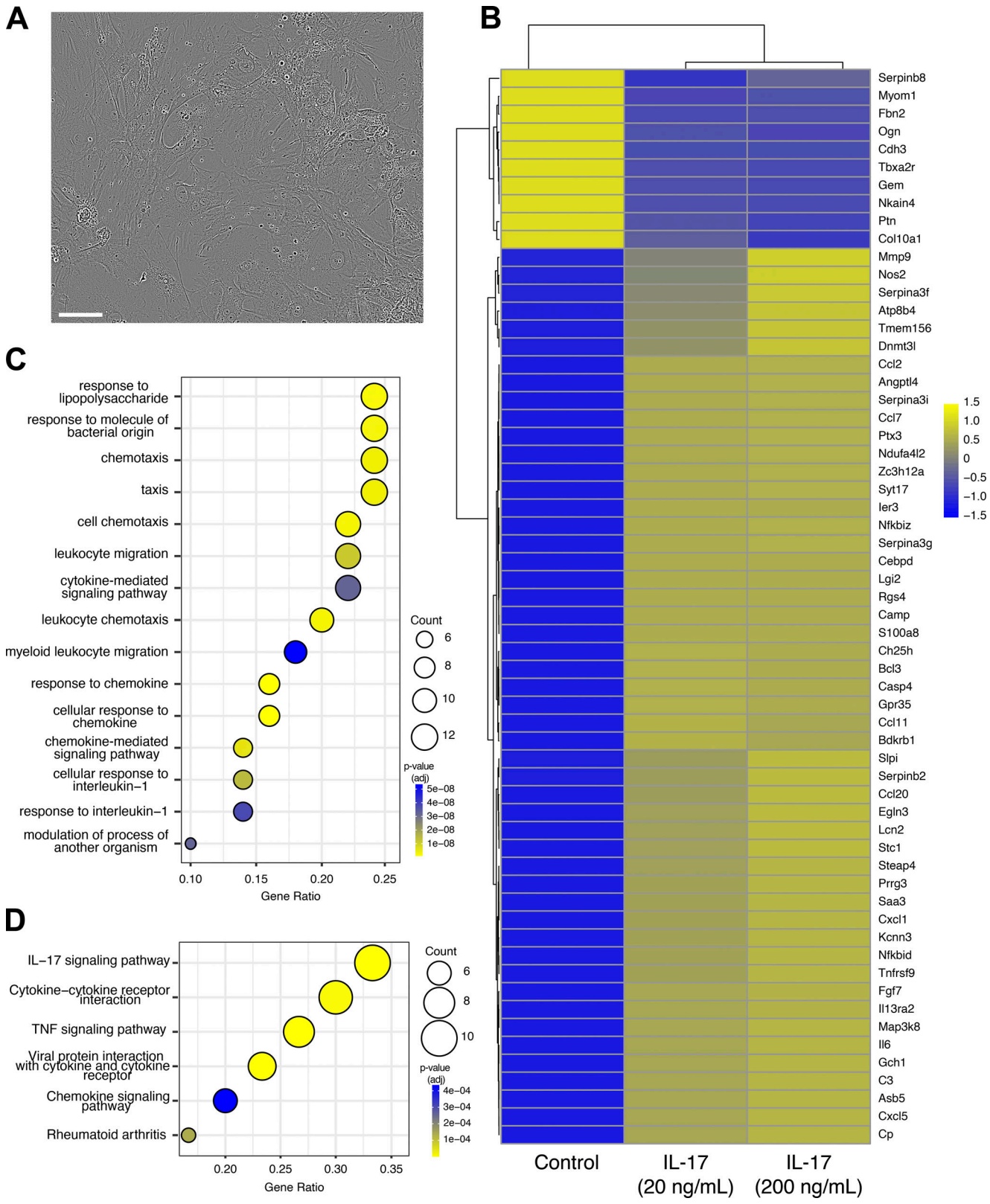

Figure 7. **IL-17A–driven transcriptional reprogramming of cecal fibroblasts sustains type 3/Th17 niche. (A)** Representative bright-field microscopy image of fibroblasts cultured from the cecum. Scale bar = 100 µm. **(B)** Heatmap of the top 50 differentially expressed genes in cecal fibroblasts following direct exposure to IL-17A at 20 and 200 ng/ml, compared with control conditions. **(C)** GO functional enrichment analysis of the top 50 differentially expressed genes. **(D)** KEGG functional enrichment analysis revealing key signaling pathways activated by IL-17. Data are presented as adjusted P values for pathway enrichment.

and is indispensable in autoimmune diseases such as experimental autoimmune encephalomyelitis (Lee et al., 2020). Additionally, we observed increased expression of *Ccl20*, the ligand for CCR6, a chemokine receptor highly expressed on mature Th17 cells and ILC3s, suggesting enhanced recruitment of these immune populations to the site of inflammation. We also observed upregulation of *Ch25h* (cholesterol 25-hydroxylase), an enzyme recently shown to be critical for the maintenance of type 3 lymphocytes, such as IL-17–producing γδ T cells, in the context of skin inflammation (Fig. 7 B) (Frascoli et al., 2023).

Gene ontology (GO) enrichment and KEGG pathway analyses revealed significant enrichment of pathways related to Th17 immunity, including responses to lipopolysaccharide and bacterial molecules, chemotaxis, leukocyte migration, chemokine signaling, cytokine–cytokine receptor interaction, and cytokine-mediated signaling. Together, these pathways suggest the presence of a sustained inflammatory feedforward loop that reinforces Th17/ILC3-driven fibrosis (Fig. 7, C and D).

In addition to heightened type 3 immunity, $Rora^{il1l7rb}$ mice displayed an increase in activated macrophages during fibrosis. IL-17A exposure upregulated genes essential for macrophage survival and inflammatory function, including *Il6*, *Ccl2*, *Ptx3*, *S100a8*, and *Nfkbiz* (Fig. 7 B). Furthermore, IL-17A–stimulated fibroblasts exhibited increased expression of *Cxcl1* and *Cxcl5*, key neutrophil chemoattractants, consistent with the established role of IL-17A in promoting neutrophil recruitment (Fig. 7, B and C).

Together, these data suggest that IL-17A signaling in fibroblasts not only fuels the Th17/ILC3 niche but also reinforces a proinflammatory microenvironment through macrophage activation and neutrophil chemotaxis, ultimately sustaining fibrosis and intestinal pathology.

The secondary bile acid, isoLCA, attenuates ILC3 and Th17 effector functions

Our data demonstrate that RORγt$^+$ ILC3 and Th17 lineages, through their production of IL-17, are the key drivers of fibrosis in response to chronic intestinal inflammation. To further explore the selective role of ILC2s and ILC3s/Th17 cells in fibrosis, we utilized the secondary bile acid metabolite, isoLCA. IsoLCA was recently shown to act as an inverse agonist of RORγt in Th17 cells through occupation of this transcription factor's ligand-binding domain, thereby dampening its ability to act as a transcriptional activator (Paik et al., 2022). Thus, it serves as a specific inhibitor of Th17 cells without affecting Th1 cells or Tregs. We hypothesized that isoLCA would show a similar activity on ILC3s, the innate counterpart to Th17 cells, and inhibit their functional capacity. A caveat, however, is that we and others showed previously that ILC3 and Th17 cells co-express RORα and RORγt (Hall et al., 2022; Lo et al., 2016; Yang et al., 2008) and these nuclear hormone receptors are known to have highly conserved ligand-binding domains and overlapping functions in regulating IL-17A/F expression (Solt and Burris, 2012). Accordingly, to clarify the relative specificity of isoLCA for these two transcription factors, we compared isoLCA's ability to attenuate reporter gene expression in RORα- and RORγt-dependent luciferase gene reporter assays. Although isoLCA exhibited a dose-dependent ability to dampen RORγ-dependent transactivation (effective concentration range 5–20 μM), it had no effect on RORα activity suggesting isoLCA is highly specific inhibitor of RORγt but not RORα (Fig. 8, A and B). It is noteworthy that in humans, secondary bile acids are normally present at sufficiently high concentrations in the intestine (~200–1,000 μM) and human feces (about 50 μM), to make this dose response to isoLCA well within the physiologically relevant range to modify intestinal immune cell functions (Hamilton et al., 2007; Paik et al., 2022).

Having validated that isoLCA is a selective inverse agonist of RORγt (Paik et al., 2022), we went on to test whether it also alters ILC3 development or function in vivo. Briefly, we generated Tg mice with RFP-labeled RORγt$^+$ cell lineages ($Rorc^{RFP}$), sorted live ILC3 and Th17 populations from $Rorc^{RFP}$ mice, and cultured these with IL-1β, with or without isoLCA (Fig. 8 C). Notably, we find isoLCA attenuates IL-17A production from both ILC3 and Th17 cells (Fig. 8 D). Since it was previously shown that isoLCA can dampen Th17 cell differentiation in vivo (Paik et al., 2022), we asked whether it similarly impacts ILC3 development. We administered isoLCA to B and T cell–deficient $Rag1^{-/-}$ mice (Fig. 8 E) and found that isoLCA profoundly suppresses IL-17A production by ILC3 and reduces the frequency of IL-17A$^+$ ILC3 cells in SI-LP (Fig. 8, F–H). In summary, our data suggest that this secondary bile acid metabolite restrains ILC3 functions in the gut through the inhibition of RORγt and specifically dampens the type 3 inflammatory program of the immune system while sparing RORα-dependent programs that are more critical for ILC2/Th2 and CD4$^+$ Treg functions.

IsoLCA inhibits IL-17A production by ILC3 and Th17 cells and protects from fibrosis

To test whether isoLCA could be used therapeutically to ameliorate gut fibrosis, we administered isoLCA to *Salmonella*-infected mice daily for 7 days, starting at a time point when signs of intestinal fibrosis first become apparent (day 14–21 after infection) (Lo et al., 2019c). We find that isoLCA significantly dampens ILC3 expansion in the SI-LP and mLN, and this also corresponds to reduced RORγt expression by ILC3 (Fig. 9, A–D) and a twofold decrease in IL-17A production by ILC3 (Fig. 9, E–G). Interestingly, we also note a significant inhibition in Th17 cell expansion as evidenced by the threefold decrease in CD4$^+$RORγt$^+$ Th17 cells (Fig. 9, H and I) and a threefold reduction in IL-17A+IFNγ+ pathogenic Th17 cells and IL-17A$^+$IFNγ$^-$ Th17 cells (Fig. 9, J and K). Notably, no significant alteration was observed in IL-17A$^-$IFNγ$^+$ Th1 cell numbers (Fig. 9 L), indicating that isoLCA specifically inhibits type 3 immunity without affecting Th1 development and function. We also observed a decrease in IL-17A gene expression in the ceca of *Salmonella*-infected mice treated orally with isoLCA (Fig. 9 M). This reduction in IL-17A gene expression correlated tightly with a decrease in fibrosis and a significant reduction in collagen deposition (Fig. 9, N and O). In summary, genetic and pharmacological inhibition of ILC3s suggests these cells play a selective, pathological role in Crohn's disease–like fibrosis, while ILC2s, in contrast, dampen susceptibility to inflammation-driven fibrosis by restraining ILC3 numbers.

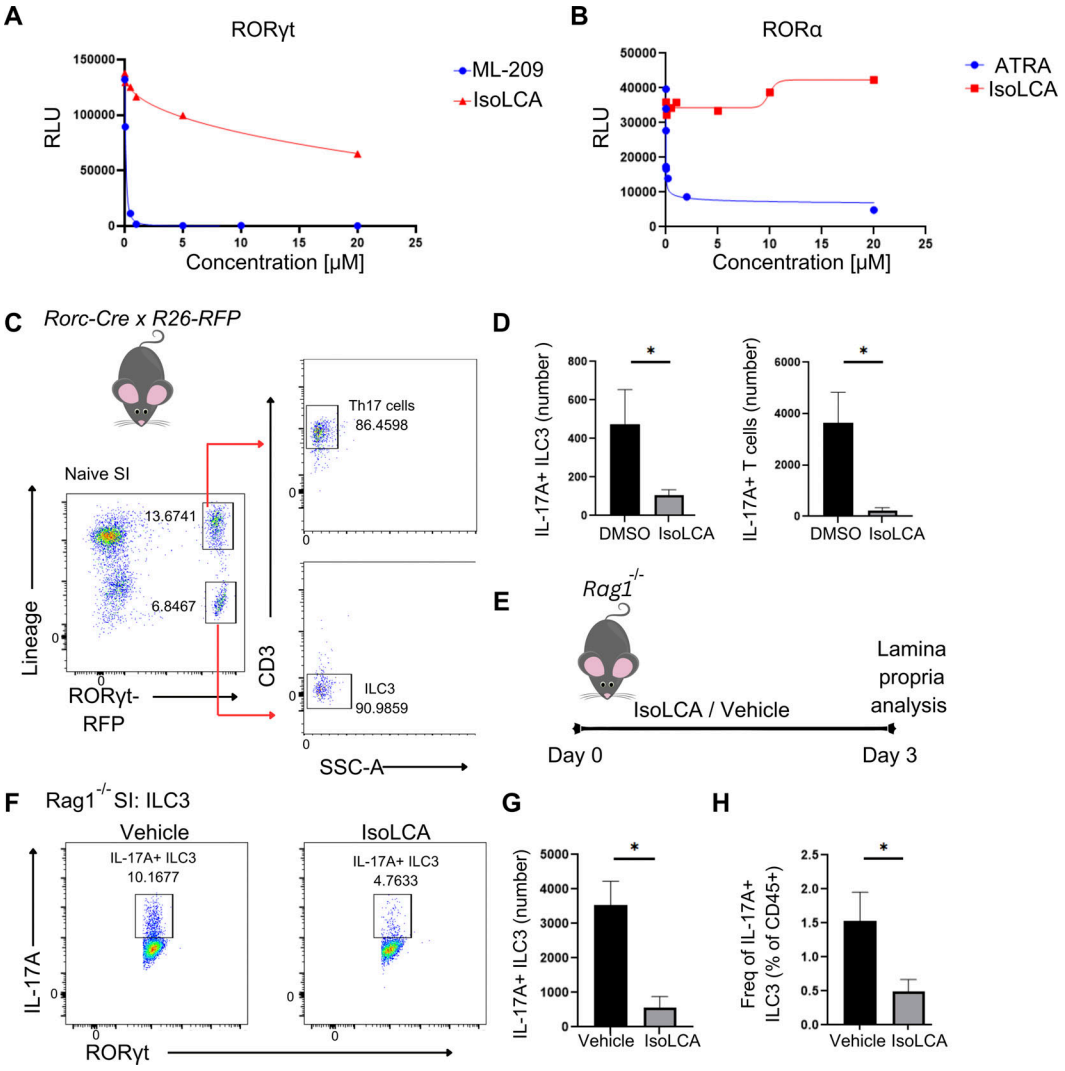

Figure 8. **Secondary bile acid isoLCA attenuates effector functions of ILC3 and Th17 cells. (A)** Inverse agonist dose–response performance of the human RORγt reporter assay system. **(B)** Inverse agonist dose–response performance of the human RORα reporter assay system. RLU, relative light units; ML-209, RORγt antagonist; ATRA, all-trans retinoic acid (RORα inverse agonist). **(C)** Fate-mapped RORγt$^+$ ILC3 and RORγt$^+$ T cells were sorted from naïve *Rorc*^{RFP} mice. **(D)** Absolute number of IL-17A$^+$ production by ILC3s and Th17 cells (n = 3 mice). ILC3 and Th17 cells were cultured with and without isoLCA + IL-1β for 3 days and stimulated with 50 ng/ml PMA (Sigma-Aldrich) and 750 ng/ml ionomycin (Sigma-Aldrich) for 4–6 h in the presence of 10 µg/ml brefeldin A (Sigma-Aldrich) in complete RPMI-1640 medium (containing 10% FBS, 50 mM 2-mercaptoethanol, 1 mM L-glutamine, 100 U/ml penicillin, and 100 µg/ml streptomycin) to assess IL-17A production by flow cytometry. **(E)** Schematic overview of the experiment design. IsoLCA was administered to *Rag1*$^{-/-}$ mice daily (oral gavage, days 0, 1, and 2) that were then euthanized on day 3. **(F)** Flow cytometry plots of IL-17A–producing live CD45$^+$Lineage$^-$RORγt$^+$ ILC3s. **(G)** Absolute numbers of IL-17A–producing ILC3s (n = 3 mice). **(H)** Frequency of Il-17A–producing ILC3s (n = 3 mice). Lineage markers: CD3ε, CD3, CD5, CD8α, TCRβ, Cd11b, CD11c, CD19, B220, Ly6C, Ly6G, Ter119. Data are representative of two independent experiments and are presented as the mean ± SEM. Statistical significance was determined using an unpaired two-tailed t test (*P < 0.05). PMA, phorbol 12-myristate 13-acetate.

Discussion

Our study provides novel insights into the selective roles of ILC2s and ILC3s in regulating intestinal homeostasis and fibrosis. Studying ILC2 and ILC3 biology has been challenging due to a lack of Tg mice that precisely target these subsets. To address this, we developed *Il17rb-CreERT2-eGFP* mice as a novel approach to selectively track ILC2s at the steady state and induce Cre-mediated gene deletion and fate mapping. Unlike recent ILC2-targeted models, such as the NMUR-Cre (Tsou et al., 2022), which lacks tamoxifen inducibility, or the Boolean-ILC2-Cre (BIC) model (Szeto et al., 2024), which requires complex multi-chromosomal intercrosses, our model provides a streamlined, tamoxifen-inducible system that enables temporal control over ILC2 deletion. This design allows for precise studies on ILC2 dynamics throughout different disease stages, offering a distinct advantage over constitutive Cre systems that risk disrupting early immune programming. Our model thus represents a valuable tool for advancing research on ILC2 and type 2 immunity. One unexpected caveat is that due to the low level of *Il17rb* gene transcription in DN2 thymocytes (sevenfold lower than in ILC2s), repeated high-dose tamoxifen treatment can result in pulse labeling of a subset of T cell progenitors and NKT cells. The fate-mapping studies performed here suggest that >95% of these cells disappear within 14 days after pulse labeling, while ILC2

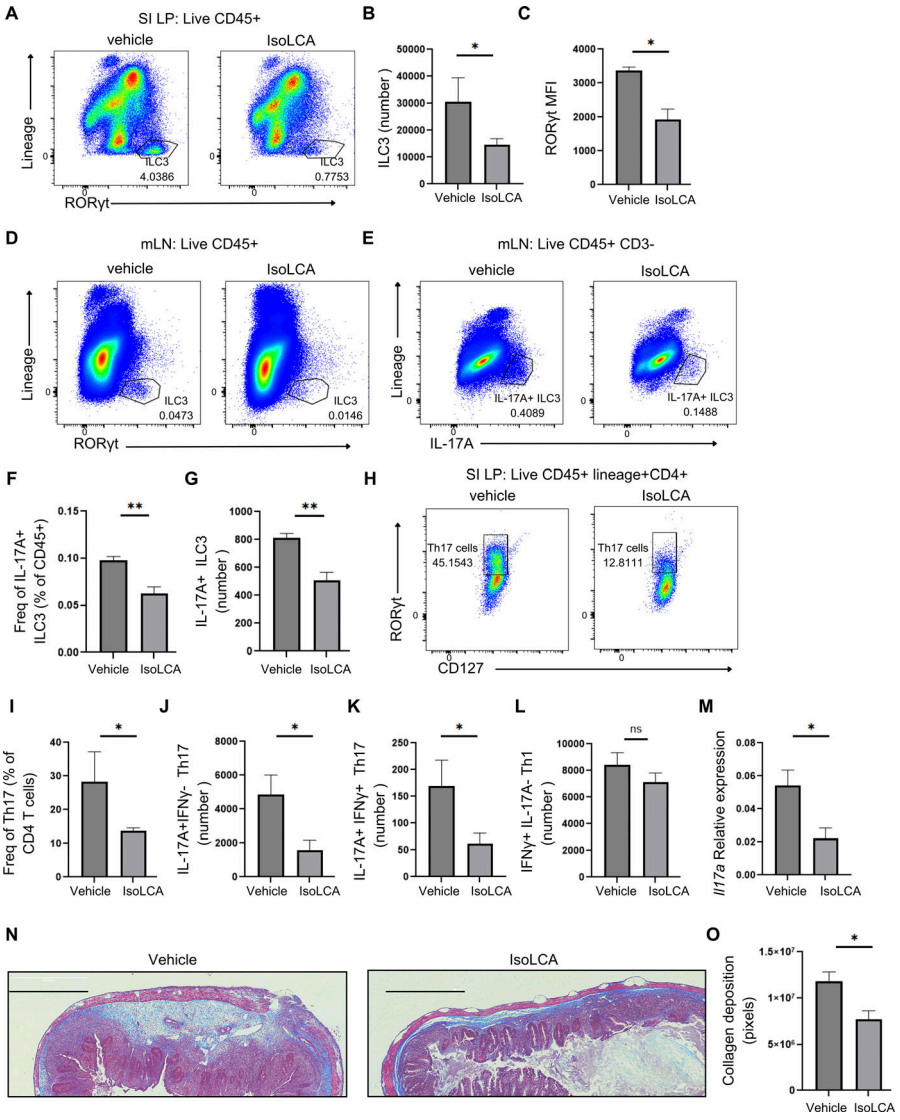

Figure 9. **IsoLCA protects from fibrosis by inhibiting IL-17A production by ILC3 and Th17 cells during intestinal inflammation.** All data presented in this figure use *Salmonella*-infected C57BL/6J-congenic mice. **(A)** Flow cytometry plots of ILC3s in the SI. **(B)** Absolute number of ILC3 (n = 3–6 mice). **(C)** MFI of RORγt by live CD45$^+$Lineage$^-$RORγt$^+$ ILC3s (n = 3–6 mice). **(D)** Flow cytometry plots of ILC3s in the mLN. **(E)** Flow cytometry plots of IL-17A production by live CD45$^+$Lineage$^-$CD3$^-$ ILC3s in the mLN. **(F)** Frequency of IL-17A$^+$ ILC3s in the mLN (n = 3–5 mice). **(G)** Number of IL-17A$^+$ ILC3 in mLN (n = 3–5 mice). **(H)** Flow cytometry plots of Th17 cells in the SI. **(I)** Frequency of Th17 cells in the SI (n = 4–5 mice). **(J)** Number of IL-17A$^+$IFNγ$^-$ Th17 cells (n = 4–5 mice). **(K)** Number of IL-17A$^+$IFNγ$^+$ pathogenic Th17 cells (n = 4–5 mice). **(L)** Number of IL-17A$^+$IFNγ$^+$ Th1 cells. **(M)** *Il17a* (IL-17A) transcript levels in ceca. **(N)** Masson's trichrome–stained cecal tissue sections. Scale bar = 1,000 µm. **(O)** Quantification of collagen deposition (n = 4–5 mice). Lineage markers: CD3ε, CD3, CD5, CD8α, TCRβ, Cd11b, CD11c, CD19, B220, Ly6C, Ly6G, Ter119. Data are representative of two independent experiments and are presented as the mean ± SEM. Statistical significance was determined using an unpaired two-tailed t test (*P < 0.05, **P < 0.01; ns, not significant). For the detection of intracellular cytokines, isolated cells were stimulated with 50 ng/ml PMA (Sigma-Aldrich) and 750 ng/ml ionomycin (Sigma-Aldrich) for 4–6 h in the presence of 10 µg/ml brefeldin A (Sigma-Aldrich) in complete RPMI-1640 medium (containing 10% FBS, 50 mM 2-mercaptoethanol, 1 mM L-glutamine, 100 U/ml penicillin, and 100 µg/ml streptomycin) to evaluate their cytokine production. PMA, phorbol 12-myristate 13-acetate.

persists lifelong. This rapid disappearance of labeled thymocytes is likely due to their progression through positive and negative selection, which ultimately results in only a small fraction (~5%) of viable naïve T cells. Nevertheless, this is an important consideration for experimental design and may also suggest additional uses for this strain in studying T cell biology and temporal turnover (unpublished data).

By leveraging the novel *Il17rb-CreERT2-eGFP* and *Rorc*-Cre deleter strains, we specifically delete RORα in ILC2s and ILC3/Th17 cells, respectively, and uncover a unique counterbalancing relationship between these cell types. The findings underscore the critical interplay, at various levels, between ILC2s, ILC3s, and Th17 cells, in intestinal fibrotic responses. Specifically, we find that selective deletion of RORα in ILC2s leads to a loss of GI ILC2s and a compensatory increase in ILC3s, resulting in elevated Th17-type immune responses and enhanced severity to Crohn's disease–like fibrosis. These observations suggest that ILC2s play an essential and underappreciated role in maintaining immune homeostasis in the gut by modulating the frequency and activity of ILC3s. Additionally, the depletion of IL-10–producing ILC2s facilitates an increase in IL-17A$^+$ Th17 cells, GM-CSF$^+$ ILC3s, and IFNγ-producing Th1 cells, leading to an elevated presence of activated macrophages in the SI. Given that *Salmonella*-infected *Rora*$^{\Delta Rorc}$ mice (with fewer ILC3s) exhibited no increase in type 2 cytokine levels, our findings suggest that general ILC subset niche occupancy does not, in and of itself, account for the heightened type 3 immune response and elevated *Il17a* expression in ILC2 deficient mice. Instead, these results point toward an immunoregulatory role of ILC2s in restraining type 3 inflammation in this context. Given that Tregs are a major source of IL-10 in the intestine, it is possible that the diminished IL-10 signal in *Il17rb-CreERT2-eGFP* × *Rora*$^{fl/fl}$ mice is also influenced by alterations in Treg homeostasis or function, as ILC2s have been implicated in supporting Treg expansion and activity (Stockis et al., 2024). However, given that our fate-mapping experiments—conducted at multiple time points up to 1 mo after tamoxifen treatment—revealed no detectable RFP labeling in Tregs, we find no evidence of a direct effect on Tregs in our deletion model. In contrast, ILC2s exhibited clear and sustained RFP labeling, reinforcing their role as the primary targeted

population. While an indirect effect on Tregs remains a possibility, any such influence would still be ILC2-dependent.

Moreover, recent studies have reported that patients with IL-10/IL10R deficiency exhibit an exacerbated Th17 response accompanied by the increased expression of RORγt by T cells (Shouval et al., 2017). While additional experiments such as Treg depletion, adoptive transfer, or conditional knockout models would be necessary to establish causality, our findings support a model in which RORα-dependent ILC2s contribute to intestinal IL-10 levels, likely through both direct and indirect mechanisms.

Our data also suggest that in the absence of ILC2s, there is a significant shift toward type 3 immunity, as evidenced by the increase in IL-17A–producing ILC3s and Th17 cells, and a corresponding increase in fibrotic pathology. These findings highlight a role of ILC2s in regulating the gut inflammatory milieu and suggest that, in some instances, the loss of ILC2 function could be a contributing factor in the development of fibrotic diseases such as Crohn's disease.

Several chronic inflammatory diseases are associated with high levels of IL-17A, and it is widely recognized that RORγt plays a pivotal role in regulating the differentiation of type 3 immune cells and the production of IL-17A (Ivanov et al., 2006). Interestingly, selective deletion of RORα in ILC3s/Th17 cells and their subsequent depletion does not significantly impact the frequency of ILC2 populations but, instead, dramatically reduces IL-17 production by ILC3s, leading to protection from fibrosis. This result is particularly intriguing as it suggests that while ILC3s are key drivers of fibrotic pathology, their activity can be modulated without affecting the overall balance of type 2 cytokines. This finding opens new avenues for targeted therapeutic interventions that could mitigate fibrosis by specific pharmacological inhibition of the RORγt pathway in ILC3s, as we demonstrate here using the RORγt inhibitor, isoLCA.

Our genetic strategies employed the targeted deletion of RORα in either ILC2 or ILC3 subsets, recognizing their shared expression and dependence on this transcription factor and the utility of this strategy in separating ILC2 and ILC3 functional activities. Very recent research has highlighted an unexpected role of RORγt^{+} APCs in the induction of tolerance, specifically in gut microbiota–specific Treg cell differentiation (Akagbosu et al., 2022; Kedmi et al., 2022; Lyu et al., 2022). Our results would argue that neither RORγt^{+} Janus cells nor ILC3s with antigen-presenting capabilities are central players in this model of intestinal fibrosis since RORα-*Cre* x MHCII$^{fl/fl}$ mice were previously shown to lack any signs of colonic inflammation or altered T cell activation states (Akagbosu et al., 2022). Thus, the sum of these collective data supports the conclusion that it is the IL-17A production directly by ILC3s, rather than their potential antigen-presenting roles, that is critical in promoting Crohn's disease–like intestinal fibrosis.

These results also substantiate our previous studies and confirm the key role of type 3 immunity in driving intestinal fibrosis. We reveal isoLCA as a naturally occurring, biologically relevant, inhibitor of RORγt in both ILC3 and Th17 but with no discernable effects on RORα function and therefore diminish concerns that pharmacological administration of isoLCA or its analogs would dampen other arms of the immune response. As a secondary, microbiome-derived, bile acid metabolite, isoLCA is ideally positioned to mitigate fibrotic susceptibility and these results could shed light on the question of why, beyond genetic factors, some individuals develop Crohn's disease with fibrostenotic strictures, while others do not. Individuals with a microbiome capable of appropriately metabolizing bile acids would be predicted to be resistant to this more severe disease sequelae. Accordingly, targeting RORγt, via isoLCA, represents a distinct therapeutic approach that warrants further investigation. Additionally, the broader applicability of isoLCA in other models of fibrosis and type 3–mediated inflammatory diseases, as well as its potential side effects, requires careful evaluation. Future studies should explore the translational potential of these findings in human diseases, particularly in the context of IBD and other fibrotic conditions.

In conclusion, our work reveals a critical counterbalancing role of ILC2s in modulating ILC3-driven immune responses in the gut, with significant implications for understanding and treating intestinal fibrosis. The identification of isoLCA as a novel inhibitor of RORγt further enhances our ability to selectively target type 3 immunity, offering new hope for therapeutic interventions in fibrotic diseases.

Materials and methods

Mice

All mice used in experiments were C57BL/6J mice (B6) (#000664; JAX) and B6-congenic (Cg) strains maintained in a specific pathogen–free facility at the Biomedical Research Centre. The *Il17rb-CreERT2-eGFP* Tg mouse line was generated through homologous recombination at the endogenous *Il17rb* locus without disrupting *Il7rb* expression (Ozgene). A linearized construct containing P2A-CreERT2-eGFP-L10a followed by a self-excising neomycin resistance cassette (neo$^{frt/frt}$) was electroporated into WT B6 ES cells. The targeted Tg was inserted between the final sense codon of *Il17rb* exon 11 and the 3′-UTR (removing the endogenous exon 11 stop codon). Neomycin-resistant ES cells were selected, and successful insertion was verified by PCR. Validated ES cells were microinjected into B6 blastocysts, which were subsequently implanted into pseudo-pregnant females. Chimeric male offspring were backcrossed with B6 females to confirm germline transmission of the transgene. F1 progeny were then crossed with FlpE-expressing B6 mice (#016226; JAX) to excise the neomycin cassette, after which the FlpE allele was eliminated and the Tg allele was maintained through continued backcrossing to B6. *Rag1*$^{-/-}$ mice (#002216; JAX) were purchased from The Jackson Laboratory. *Rorc*^{RFP} mice were generated by crossing *Rorc*-Cre with R26-tdRFP mice (experimental mice were heterozygous for both Cre and RFP alleles). All strains were housed in autoclaved cages and received irradiated chow ad libitum (equal parts mixture of PicoLab Mouse Diet 20 and Picolab Rodent Diet 20) and autoclaved tap water. All experiments were carried out humanely in accordance with the Canadian Council on Animal Care guidelines and were approved by the University of British Columbia Committee on Animal Care (A21-0132 [isoLCA treatment], A22-0111 [necropsy], and A23-0145 [RG2 *Salmonella* infection

model]). At experimental endpoints, mice were euthanized by Avertin (2,2,2-tribromoethanol) overdose or controlled-delivery CO_2 asphyxiation.

IsoLCA in vivo study design

For oral bile acid administration, mice received isoLCA (BenchChem) at a concentration of 70 mg/kg body weight or vehicle (oil) daily for 3 days by oral gavage (naïve *Rag1*$^{-/-}$ mice) or 7 days (*Salmonella*-infected B6-Cg mice).

Salmonella ΔA*roA* fibrosis model

Growth of the *Salmonella* Δ*AroA* strain (streptomycin-resistant [StrepR] serovar Typhimurium SL1344), infection of mice, and the fibrosis model were conducted as previously described (Lo et al., 2016, 2019c). Mice were treated (by oral gavage) with 150 µl of streptomycin (200 mg/ml) 24 h before oral gavage infection with 3 × 10^6 Sal Δ*AroA* colony-forming units (CFU) resuspended in 100 µl of phosphate-buffered saline (PBS). Mouse weights were assessed every 4 days. At day 21 after infection, mice were euthanized, and tissues were collected for analysis and bacterial enumeration. Cecal tissue was homogenized in sterile PBS, and serial dilutions were placed on LB agar plates (streptomycin [100 µg/ml]) to enumerate Sal Δ*AroA* CFU.

Tamoxifen treatments

To induce CreERT2 nuclear translocation, adult mice were injected intraperitoneally (i.p.) with 100 mg/kg of tamoxifen in 100 µl sunflower oil daily for 5 consecutive days followed by a 7–14-day washout period. Neonatal pups were injected i.p. with 400 µg for 3 consecutive days.

Histology

Ceca were collected and fixed in 10% formalin overnight on a shaker (room temperature), and then transferred to tubes with 70% ethanol. Fixed tissues were embedded in paraffin and cut into 5-µm section for Mason's trichrome staining by Wax-It Histology Services. Sections were then imaged using Nikon Eclipse Microscope with consistent exposure settings across all samples and analyzed and quantified using Fiji by ImageJ, where personnel outlined the outer and inner boundaries of collagen deposition across the ceca, notably deposited on the borders. Collagen deposition was noted through its blue staining, where regions with higher collagen density appeared as dark blue, while areas with less deposition were lighter blue. Collagen deposition area was thus determined by calculating the difference between the outlined outer and inner regions. Variations in inflammation and deposition patterns may have led to a few smaller dark blue regions potentially being underrepresented in the overall quantification.

To quantify epithelial shedding, we measured the percentage of the luminal surface area exhibiting a delaminated yet intact epithelial layer in histological sections. This was done using ImageJ/Fiji software, where the total length of the epithelial layer lining the lumen was traced and compared with the length of the visibly detached, but continuous, epithelial sheet. Based on these measurements, we established the following scoring system: Score 0: 0–5% of the luminal surface exhibits shedding; Score 1: 5–25% shedding; Score 2: 25–50% shedding; Score 3: 50–75% shedding; Score 4: >75% shedding.

For eGFP detection by immunofluorescence histology, tissue samples were fixed in 4% paraformaldehyde for 1–2 h, washed in PBS, embedded in paraffin, and sectioned at 5–10 µm. Sections were deparaffinized in xylene, rehydrated in graded ethanol, and rinsed in distilled water. Antigen retrieval was performed using BOND Epitope Retrieval Solution 2 (EDTA-based, pH 9.0) for 20 min. After cooling and PBS washing, sections were blocked with 5% serum for 30 min. Primary anti-GFP antibody (ab183734; Abcam) diluted 1:75 in Bond Diluent was applied, and sections were incubated at 4°C for 8 h. Following PBS washes, a fluorescent-conjugated secondary antibody was applied for 1 h at room temperature. Final PBS washes were done before mounting with DAPI-containing medium. Imaging was conducted using a fluorescence microscope.

Cell preparation and flow cytometry

The SI was digested using collagenase VIII (Sigma-Aldrich). Briefly, the SI was dissected from below the stomach and above the cecum and then placed in a petri dish containing HBSS (Gibco), 5% fetal bovine serum (FBS; Sigma-Aldrich). The fecal contents were washed out, and fat was removed before the SI was cut longitudinally and cut into small pieces. The SI was then placed in HBSS, 5% FBS and shaken vigorously, before being filtered and placed in 20–30 ml of HBSS, 5% FBS, 2.5 mM EDTA, 1 mM DL-Dithiothreitol (DTT). Each SI was then incubated and shaken at 37°C for 20 min. The SI underwent a second round of incubation at 37°C for 20 min in 20–30 ml of HBSS, 5% FBS, 2.5 mM EDTA, 1 mM DTT. The SI was then filtered and incubated at 37°C for 20 min in 20 ml of HBSS (no EDTA). The SI was then incubated for 15 min at 37°C in 1.5 mg/ml type VIII collagenase (Sigma-Aldrich) dissolved in prewarmed RPMI 1640, 10% FBS with 40 µg/ml of DNase I (10104159001; Roche). The SI was filtered through 100-µm and 70-µm cell strainers before being centrifuged and resuspended in an appropriate amount of PBS containing 2% fetal calf serum, 2 mM EDTA, and 0.05% sodium azide (when cells were stained straightaway) or culture medium (when cells were cultured and stimulated in vitro before staining). Lungs were chopped into small pieces and digested with Liberase (working concentration, 42.4 mg/ml) and DNase I (working concentration, 0.05 mg/ml) in RPMI 1640, 10% FBS for 40 min at 37°C; then, the entire digested tissue was pressed through a 40-µm cell strainer to obtain single-cell suspensions. ACK lysis buffer was used to lyse red blood cells. Staining and antibody dilutions were prepared in fluorescence-activated cell sorting buffer (PBS containing 2% FBS and 2 mM EDTA). Ear skin samples were processed to obtain single-cell suspensions for flow cytometry analysis. Briefly, ears were excised using dissection scissors along the hairline and placed in 1.5 ml RPMI + 5% FBS. The tissue was further cut into small sections and incubated in ear digestion solution containing 300 µg/ml Liberase and 50 U/ml DNase I in RPMI with 5% FBS. Samples were vortexed to resuspend in media and incubated at 37°C for 90 min with agitation. Following digestion, cell suspensions were passed through a 70-µm cell strainer into a 50-ml Falcon tube, and the strainer was washed with 5 ml DMEM to collect residual

cells. Cells were centrifuged, filtered if necessary, and resuspended in FACS buffer for downstream flow cytometry analysis. To extract BM, a 0.5-ml microcentrifuge tube was prepared by puncturing a hole in the bottom using an 18 G blunt needle. Bones were cut open at one end and placed cut-side down into the prepared tube. Each 1.5-ml microcentrifuge tube was prefilled with 100 µl media, and the 0.5-ml tube containing bones was inserted into it before closing the lid. Samples were then centrifuged at 2,500 × *g* for 1 min at room temperature to expel BM into the collection tube. If necessary, an additional spin or recutting of bones was performed to ensure maximal marrow extraction. Lymph nodes/Peyer's patches were placed in cold RPMI + 5% FBS. Lymph nodes were mechanically dissociated by pressing them through a 70-µm strainer using the flat end of a 1-ml syringe plunger, followed by rinsing with 2–3 ml RPMI to maximize cell recovery. The suspension was collected in a 15-ml Falcon tube, centrifuged at 300 × *g* for 5 min at 4°C, and resuspended in FACS buffer. If needed, the suspension was passed through a fresh 70-µm filter to remove clumps before downstream applications. Muscles were dissected and digested with collagenase II and Dispase. Dissociated muscles were passed through a 70-µm filter, and red blood cells were lysed in ACK lysis buffer. Cells were incubated with LIVE/DEAD fixable dead cell stain dye followed by fluorochrome-conjugated antibodies. Staining and washing were performed at 4°C. For intracellular cytokine staining, cells were fixed with either Transcription Factor Fixation/Permeabilization Buffer Set (cat. no. 424401) or Cytofix/Cytoperm 1× solution (cat. no. 554722; BD Biosciences) for cell fixation to preserve eGFP and RFP signal and subsequently stained with fluorochrome-conjugated antibodies for transcription factors and cytokines in 1× permeabilization buffer. Cells were analyzed on a CytoFLEX LX flow cytometer, and data were analyzed with FlowJo software. Cell numbers were calculated based on flow cytometry data by staining each sample with 1 ml of staining buffer, plating 100–200 µl, and recording an equal volume on the cytometer. The number of cells per microliter was determined from the recorded events and used to calculate total cell counts.

Reporter assay system

To test the impact of isoLCA on RORγ and RORα transcriptional activation, we used human RAR-related orphan receptor gamma (Product #IB04001-32; INDIGO Biosciences) and human RAR-related orphan receptor alpha (Product #IB04011-32; INDIGO Biosciences) cell-based reporter assays following the manufacturer's protocol.

IL-33–induced allergic lung inflammation

PBS vehicle control or IL-33 (0.5 µg) (Thermo Fisher Scientific, Waltham, Mass; or BioLegend) was administered to mice intranasally daily for 3 days (days 0, 1, and 2), then euthanized on day 3. All stock concentrations delivered to adult mice were diluted in sterile PBS to achieve working concentrations.

Reverse transcriptase quantitative PCR

Total RNA was extracted from cecal tissue section using TRIzol (Invitrogen), and purity was quantified using a NanoDrop system. The RNA was diluted to 200 ng/µl and then reverse-transcribed with a high-capacity complementary DNA reverse transcription kit (Applied Biosystems). Quantitative real-time polymerase chain reaction was performed using SYBR Luna MasterMix (New England BioLabs) using the ABI 7900 real-time PCR instrument (Life Technologies). Primer sequences were as follows: β-actin forward 5′-ACTAATGGCAACGAGCGGTTC-3′ and reverse 5′-GGATGCCACAGGATTCCATACC-3′; *Gapdh* forward 5′-AGGTCGGTGTGAACGGATTTG-3′ and reverse 5′-TGTAGACCATGTAGTTGAGGTCA-3′; *Il5* forward 5′-CTCTGTTGACAAGCAATGAGACG-3′ and reverse 5′-TCTTCAGTATGTCTAGCCCCTG-3′; *Il3* forward 5′-CCTGGCTCTTGCTTGCCTT-3′ and reverse 5′-GGTCTTGTGTGATGTTGCTCA-3′; *Il17a* forward 5′-TTTAACTCCCTTGGCGCAAAA-3′ and reverse 5′-CTTTCCCTCCGCATTGACAC-3′. *Col3a1* forward 5′-CTGTAACATGAAACTGGGGAAA-3′ and reverse 5′-CCATAGCTGAACTGAAAACCACC-3′.

Tissue dissociation for primary fibroblast cultures

Primary intestinal fibroblast cultures were prepared as previously described (Pandey et al., 2023), with a few modifications. Briefly, cecum and large intestine were harvested from PdgfraEGFP mice, exterior fat was removed, and tissues were placed on ice in a petri dish containing PBS. An 18G needle and syringe were used to flush the lumen with cold PBS, the tissue was cut longitudinally to expose the lumen, and a microscope slide was used to scrape mucus from the luminal side. The tissue was cut into ∼5-mm pieces, placed into a 50-ml tube containing cold PBS, and agitated to remove any residual luminal contents. After allowing tissue to settle, the supernatant was discarded and two additional washes were completed. To remove epithelial cells, 25 ml of HBSS (14170; Gibco) extraction solution (containing 10 mM EDTA and 12.5 µl/ml of 1 M dithiothreitol) was added and tissues were incubated at 37°C for 15 min with rigorous shaking (250 rpm). The supernatant was decanted, and epithelial cell extraction was repeated. Following the second extraction, the solution was filtered using a 70-µm strainer, and unfiltered tissue pieces were rinsed with 20 ml of prewarmed PBS. Sterile forceps were used to move tissue pieces into a 15-ml tube containing 5 ml of digest solution (4 mg/ml collagenase D [11088882001; Roche], 2.5 mg/ml Pronase [10165921001; Roche], DNase I [11284932001], 10 µl/ml 250 mM $CaCl_2$), and incubated for 30 min at 37°C with shaking (250 rpm). A 70-µm strainer was used to filter the digested cell suspension, and 20 ml of cell culture media (DMEM [11965; Gibco] containing 20% FBS [12483; Gibco], L-glutamine [25030; Gibco], and penicillin–streptomycin [15140; Gibco]) was added prior to centrifugation at 4°C for 5 min at 500 × *g*. After the supernatant was removed, 10 ml of filter-sterilized ACK lysing buffer (A10892; Gibco) was used to resuspend the cell pellet, followed by centrifugation as above. Once the supernatant was removed, cells were resuspended in cell culture media, added to a T-75 flask, and incubated overnight. The following day, fresh media were added, and fibroblasts were maintained as per standard cell culture practices.

Treatment of fibroblasts with IL-17 and RNA extraction

Once sufficiently expanded, fibroblasts were seeded into 24-well plates. The next day, images were taken of each well using a

CellCyte X (Cytena) and cells were treated, in duplicate, with either 20 or 200 ng/ml of IL-17A (576006; BioLegend), or an equivalent volume of 1% BSA in PBS as a control. After 24 h, each well was washed with PBS and cells were lysed using buffer RLT (Qiagen) and QIAshredder columns (79656; Qiagen). RNA was isolated using RNeasy mini kits (74106; Qiagen), as per the manufacturer's instructions.

Population RNA sequencing

RNA quality was assessed with an Agilent TapeStation 4200. Libraries were generated from RNA samples with an RNA Integrity Number >8, using the standard TruSeq Stranded mRNA library kit protocol. Paired-end sequencing was performed on the Illumina NextSeq 2000 using the P4 100 cycle kit.

RNA-seq bioinformatics analyses

Illumina sequencing outputs generated bcl files that were demultiplexed by bcl2fastq2. Demultiplexed read sequences were aligned to the mouse genome (mm10) reference sequence using TopHat58 splice junction mapper with Bowtie 259 or STAR60 aligners (RNA-seq Alignment app, Illumina BaseSpace). DESeq2 was used for the identification and statistical validation of differentially expressed genes. To perform DESeq2 analysis, untreated control cells were compared with IL-17A–treated cells (combine 20 and 200 ng/ml doses). Differentially expressed genes (adjusted $P < 0.05$) were ordered based on $\log_2$ fold change, and the top 10 downregulated and top 50 upregulated genes were included in a heatmap. Hierarchical clustering of population RNA-seq data and heatmap generation were performed with the pheatmap R package using the Euclidian distance. For gene set enrichment results, the top 50 upregulated genes were subjected to GO biological processes and KEGG pathway analyses, and the top hits were plotted in R using ggplot2. The software used to analyze the data is either freely or commercially available.

Statistics

Unless otherwise specified, differences between treatment groups were compared using a paired and unpaired Student's *t* test, as appropriate, or one-way ANOVA (GraphPad Prism Software, version 4.0, CA). Error bars are the SEM unless otherwise stated.

Online supplemental material

Fig. S1 shows that *Il17rb* is uniformly expressed by tissue ILC2s, as determined by scRNA-seq analyses of intestinal ILCs from steady-state and inflamed conditions, as well as publicly available transcriptomics data from ImmGen. Fig. S2 shows *Il17rb* expression across multiple thymic cell populations. Fig. S3 shows *Il17rb* expression in the BM and during IL-33–induced type 2 inflammation. Fig. S4 shows that early-life deletion of RORα in ILC2s leads to reduced ILC2 numbers and cytokine production in adulthood. Fig. S5 shows that RORα deletion in ILC3/Th17 cells has no effect on ILC2 numbers but is required for the development of a subset of ILC3s, as determined by scRNA-seq analysis of $Rora^{sg/sg}$ mice.

Data availability

All data necessary to understand and evaluate the conclusions of this paper are provided in the published article or the supplemental material. The fibroblast RNA-seq dataset is available in the GEO repository with the accession number GSE290467.

Acknowledgments

The authors thank the core facilities of the Biomedical Research Centre for critical technical support with special thanks to Krista Ranta, Wei Yuan, and Marcelo Paixao in the BRC Tg facility for animal welfare support, Taka Murakami and the UBC Genotyping Core, Andy Johnson and the UBC Flow Cytometry Facility, and Tara Stach at the UBC SBME Sequencing Facility. This work benefited from data assembled by the ImmGen consortium. We acknowledge that the land on which this work was conducted is the unceded, ancestral, and rightful territory of the Sḵwx̱wú7mesh (Squamish), səlilw̓ətaʔɬ (Tsleil-Waututh), and xʷməθkʷəy̓əm (Musqueam) Nations and offer our gratitude for the opportunity to work and learn there.

This work was supported by project grants PJT-518208 and PJT-4488212 from the Canadian Institutes of Health Research (CIHR) to K.M. McNagny and Canadian Microbiome Team Grants MRT-168048 and MRT168044 from CIHR. A. Kabil was supported by an NSERC Vanier Scholarship, and J. Brassard is supported by a postdoctoral award from the Michael Smith Foundation of Health Research.

Author contributions: A. Kabil: conceptualization, data curation, formal analysis, funding acquisition, investigation, methodology, software, validation, visualization, and writing—original draft, review, and editing. N. Nayyar: investigation and writing—original draft. C. Xu: investigation. J. Brassard: conceptualization, investigation, and writing—review and editing. L.A. Hill: data curation, formal analysis, investigation, methodology, resources, and visualization. S.B. Shin: conceptualization, methodology, supervision, and writing—review and editing. S. Chopra: conceptualization, investigation, methodology, validation, and writing—review and editing. B. Lo: investigation and methodology. Y. Li: writing—review and editing. M. Bal: investigation. M. Theret: investigation and validation. F. Rossi: funding acquisition and supervision. T.M. Underhill: methodology, project administration, resources, supervision, and writing—review and editing. M.R. Hughes: conceptualization, funding acquisition, methodology, project administration, supervision, validation, and writing—review and editing. K.M. McNagny: conceptualization, funding acquisition, methodology, project administration, resources, supervision, and writing—review and editing.

Disclosures: T.M. Underhill owns stock in two biotechnology companies, Mesentech, Inc. and Mesintel Therapeutics, Inc. No other disclosures were reported.

Submitted: 10 September 2024
Revised: 6 March 2025
Accepted: 28 April 2025

References

Akagbosu, B., Z. Tayyebi, G. Shibu, Y.A. Paucar Iza, D. Deep, Y.F. Parisotto, L. Fisher, H.A. Pasolli, V. Thevin, R. Elmentaite, et al. 2022. Novel antigen-presenting cell imparts T_{reg}-dependent tolerance to gut microbiota. *Nature*. 610:752–760. https://doi.org/10.1038/s41586-022-05309-5

Araujo, L.P., M. Edwards, K. Irie, Y. Huang, Y. Kawano, A. Tran, S. De Michele, G. Bhagat, H.H. Wang, and I.I. Ivanov. 2024. Context-dependent role of group 3 innate lymphoid cells in mucosal protection. *Sci. Immunol.* 9:eade7530. https://doi.org/10.1126/sciimmunol.ade7530

Arifuzzaman, M., T.H. Won, H. Yano, J. Uddin, E.R. Emanuel, E. Hu, W. Zhang, T.T. Li, W.B. Jin, A. Grier, et al. 2024. Dietary fiber is a critical determinant of pathologic ILC2 responses and intestinal inflammation. *J. Exp. Med.* 221:e20232148. https://doi.org/10.1084/jem.20232148

Bando, J.K., S. Gilfillan, B. Di Luccia, J.L. Fachi, C. Secca, M. Cella, and M. Colonna. 2020. ILC2s are the predominant source of intestinal ILC-derived IL-10. *J. Exp. Med.* 217:e20191520. https://doi.org/10.1084/jem.20191520

Benoist, C., L. Lanier, M. Merad, D. Mathis, and Immunological Genome Project. 2012. Consortium biology in immunology: The perspective from the immunological Genome project. *Nat. Rev. Immunol.* 12:734–740. https://doi.org/10.1038/nri3300

Bielecki, P., S.J. Riesenfeld, J.C. Hütter, E. Torlai Triglia, M.S. Kowalczyk, R.R. Ricardo-Gonzalez, M. Lian, M.C. Amezcua Vesely, L. Kroehling, H. Xu, et al. 2021. Skin-resident innate lymphoid cells converge on a pathogenic effector state. *Nature*. 592:128–132. https://doi.org/10.1038/s41586-021-03188-w

Buonocore, S., P.P. Ahern, H.H. Uhlig, I.I. Ivanov, D.R. Littman, K.J. Maloy, and F. Powrie. 2010. Innate lymphoid cells drive interleukin-23-dependent innate intestinal pathology. *Nature*. 464:1371–1375. https://doi.org/10.1038/nature08949

Castro-Dopico, T., A. Fleming, T.W. Dennison, J.R. Ferdinand, K. Harcourt, B.J. Stewart, Z. Cader, Z.K. Tuong, C. Jing, L.S.C. Lok, et al. 2020. GM-CSF calibrates macrophage defense and wound healing programs during intestinal infection and inflammation. *Cell Rep.* 32:107857. https://doi.org/10.1016/j.celrep.2020.107857

Cording, S., J. Medvedovic, E. Lécuyer, T. Aychek, F. Déjardin, and G. Eberl. 2018. Mouse models for the study of fate and function of innate lymphoid cells. *Eur. J. Immunol.* 48:1271–1280. https://doi.org/10.1002/eji.201747388

Eberl, G., M. Colonna, J.P. Di Santo, and A.N. McKenzie. 2015. Innate lymphoid cells. Innate lymphoid cells: A new paradigm in immunology. *Science*. 348:aaa6566. https://doi.org/10.1126/science.aaa6566

Eberl, G., and D.R. Littman. 2004. Thymic origin of intestinal alphabeta T cells revealed by fate mapping of RORgammat+ cells. *Science*. 305:248–251. https://doi.org/10.1126/science.1096472

Eberl, G., S. Marmon, M.J. Sunshine, P.D. Rennert, Y. Choi, and D.R. Littman. 2004. An essential function for the nuclear receptor RORgamma(t) in the generation of fetal lymphoid tissue inducer cells. *Nat. Immunol.* 5:64–73. https://doi.org/10.1038/ni1022

Ehrhardt, K., N. Steck, R. Kappelhoff, S. Stein, F. Rieder, I.O. Gordon, E.C. Boyle, P. Braubach, C.M. Overall, B.B. Finlay, and G.A. Grassl. 2019. Persistent Salmonella enterica serovar Typhimurium infection induces protease expression during intestinal fibrosis. *Inflamm. Bowel Dis.* 25:1629–1643. https://doi.org/10.1093/ibd/izz070

Fiancette, R., C.M. Finlay, C. Willis, S.L. Bevington, J. Soley, S.T.H. Ng, S.M. Baker, S. Andrews, M.R. Hepworth, and D.R. Withers. 2021. Reciprocal transcription factor networks govern tissue-resident ILC3 subset function and identity. *Nat. Immunol.* 22:1245–1255. https://doi.org/10.1038/s41590-021-01024-x

Frascoli, M., E. Ferraj, B. Miu, J. Malin, N.A. Spidale, J. Cowan, S.C. Shissler, R. Brink, Y. Xu, J.G. Cyster, et al. 2023. Skin γδ T cell inflammatory responses are hardwired in the thymus by oxysterol sensing via GPR183 and calibrated by dietary cholesterol. *Immunity*. 56:562–575.e6. https://doi.org/10.1016/j.immuni.2023.01.025

Glocker, E.O., D. Kotlarz, K. Boztug, E.M. Gertz, A.A. Schäffer, F. Noyan, M. Perro, J. Diestelhorst, A. Allroth, D. Murugan, et al. 2009. Inflammatory bowel disease and mutations affecting the interleukin-10 receptor. *N. Engl. J. Med.* 361:2033–2045. https://doi.org/10.1056/NEJMoa0907206

Gold, M.J., F. Antignano, T.Y. Halim, J.A. Hirota, M.R. Blanchet, C. Zaph, F. Takei, and K.M. McNagny. 2014. Group 2 innate lymphoid cells facilitate sensitization to local, but not systemic, TH2-inducing allergen exposures. *J. Allergy Clin. Immunol.* 133:1142–1148. https://doi.org/10.1016/j.jaci.2014.02.033

Grassl, G.A., Y. Valdez, K.S. Bergstrom, B.A. Vallance, and B.B. Finlay. 2008. Chronic enteric salmonella infection in mice leads to severe and persistent intestinal fibrosis. *Gastroenterology*. 134:768–780. https://doi.org/10.1053/j.gastro.2007.12.043

Griseri, T., B.S. McKenzie, C. Schiering, and F. Powrie. 2012. Dysregulated hematopoietic stem and progenitor cell activity promotes interleukin-23-driven chronic intestinal inflammation. *Immunity*. 37:1116–1129. https://doi.org/10.1016/j.immuni.2012.08.025

Guo, B. 2016. IL-10 modulates Th17 pathogenicity during autoimmune diseases. *J. Clin. Cell Immunol.* 7:400. https://doi.org/10.4172/2155-9899.1000400

Gury-BenAri, M., C.A. Thaiss, N. Serafini, D.R. Winter, A. Giladi, D. Lara-Astiaso, M. Levy, T.M. Salame, A. Weiner, E. David, et al. 2016. The spectrum and regulatory landscape of intestinal innate lymphoid cells are shaped by the microbiome. *Cell*. 166:1231–1246.e13. https://doi.org/10.1016/j.cell.2016.07.043

Halim, T.Y., R.H. Krauss, A.C. Sun, and F. Takei. 2012. Lung natural helper cells are a critical source of Th2 cell-type cytokines in protease allergen-induced airway inflammation. *Immunity*. 36:451–463. https://doi.org/10.1016/j.immuni.2011.12.020

Halim, T.Y., C.A. Steer, L. Mathä, M.J. Gold, I. Martinez-Gonzalez, K.M. McNagny, A.N. McKenzie, and F. Takei. 2014. Group 2 innate lymphoid cells are critical for the initiation of adaptive T helper 2 cell-mediated allergic lung inflammation. *Immunity*. 40:425–435. https://doi.org/10.1016/j.immuni.2014.01.011

Hall, J.A., M. Pokrovskii, L. Kroehling, B.R. Kim, S.Y. Kim, L. Wu, J.Y. Lee, and D.R. Littman. 2022. Transcription factor RORα enforces stability of the Th17 cell effector program by binding to a Rorc cis-regulatory element. *Immunity*. 55:2027–2043.e9. https://doi.org/10.1016/j.immuni.2022.09.013

Hamilton, J.P., G. Xie, J.P. Raufman, S. Hogan, T.L. Griffin, C.A. Packard, D.A. Chatfield, L.R. Hagey, J.H. Steinbach, and A.F. Hofmann. 2007. Human cecal bile acids: Concentration and spectrum. *Am. J. Physiol. Gastrointest. Liver Physiol.* 293:G256–G263. https://doi.org/10.1152/ajpgi.00027.2007

Ivanov, I.I., B.S. McKenzie, L. Zhou, C.E. Tadokoro, A. Lepelley, J.J. Lafaille, D.J. Cua, and D.R. Littman. 2006. The orphan nuclear receptor RORgammat directs the differentiation program of proinflammatory IL-17+ T helper cells. *Cell*. 126:1121–1133. https://doi.org/10.1016/j.cell.2006.07.035

Jacquelot, N., C. Seillet, M. Wang, A. Pizzolla, Y. Liao, S. Hediyeh-Zadeh, S. Grisaru-Tal, C. Louis, Q. Huang, J. Schreuder, et al. 2021. Blockade of the co-inhibitory molecule PD-1 unleashes ILC2-dependent antitumor immunity in melanoma. *Nat. Immunol.* 22:851–864. https://doi.org/10.1038/s41590-021-00943-z

Jan-Abu, S.C., A. Kabil, and K.M. McNagny. 2023. Parallel origins and functions of T cells and ILCs. *Clin. Exp. Immunol.* 213:76–86. https://doi.org/10.1093/cei/uxad056

Jou, E., N. Rodriguez-Rodriguez, A.F. Ferreira, H.E. Jolin, P.A. Clark, K. Sawmynaden, M. Ko, J.E. Murphy, J. Mannion, C. Ward, et al. 2022. An innate IL-25-ILC2-MDSC axis creates a cancer-permissive microenvironment for Apc mutation-driven intestinal tumorigenesis. *Sci. Immunol.* 7:eabn0175. https://doi.org/10.1126/sciimmunol.abn0175

Kabil, A., S.B. Shin, M.R. Hughes, and K.M. McNagny. 2022. "Just one word, plastic!": Controversies and caveats in innate lymphoid cell plasticity. *Front. Immunol.* 13:946905. https://doi.org/10.3389/fimmu.2022.946905

Kedmi, R., T.A. Najar, K.R. Mesa, A. Grayson, L. Kroehling, Y. Hao, S. Hao, M. Pokrovskii, M. Xu, J. Talbot, et al. 2022. A RORγt$^+$ cell instructs gut microbiota-specific T_{reg} cell differentiation. *Nature*. 610:737–743. https://doi.org/10.1038/s41586-022-05089-y

Kiner, E., E. Willie, B. Vijaykumar, K. Chowdhary, H. Schmutz, J. Chandler, A. Schnell, P.I. Thakore, G. LeGros, S. Mostafavi, et al. 2021. Gut CD4$^+$ T cell phenotypes are a continuum molded by microbes, not by T_H archetypes. *Nat. Immunol.* 22:216–228. https://doi.org/10.1038/s41590-020-00836-7

Lee, J.-Y., J.A. Hall, L. Kroehling, L. Wu, T. Najar, H.H. Nguyen, W.-Y. Lin, S.T. Yeung, H.M. Silva, D. Li, et al. 2020. Serum amyloid A proteins induce pathogenic Th17 cells and promote inflammatory disease. *Cell*. 180:79–91.e16. https://doi.org/10.1016/j.cell.2019.11.026

Lo, B.C., S.B. Shin, D. Canals Hernaez, I. Refaeli, H.B. Yu, V. Goebeler, A. Cait, W.W. Mohn, B.A. Vallance, and K.M. McNagny. 2016. The orphan nuclear receptor ROR alpha and group 3 innate lymphoid cells drive fibrosis in a mouse model of Crohn's disease. *Sci. Immunol.* 1:eaaf8864. https://doi.org/10.1126/sciimmunol.aaf8864

Lo, B.C., D. Canals Hernaez, R.W. Scott, M.R. Hughes, S.B. Shin, T.M. Underhill, F. Takei, and K.M. McNagny. 2019a. The transcription factor

RORα preserves ILC3 lineage identity and function during chronic intestinal infection. *J. Immunol.* 203:3209–3215. https://doi.org/10.4049/jimmunol.1900781

Lo, B.C., S.B. Shin, D. Canals Hernaez, I. Refaeli, H.B. Yu, V. Goebeler, A. Cait, W.W. Mohn, B.A. Vallance, and K.M. McNagny. 2019b. IL-22 preserves gut epithelial integrity and promotes disease remission during chronic Salmonella infection. *J. Immunol.* 202:956–965. https://doi.org/10.4049/jimmunol.1801308

Lo, B.C., S.B. Shin, M. Messing, and K.M. McNagny. 2019c. Chronic Salmonella infection induced intestinal fibrosis. *J. Vis. Exp.* https://doi.org/10.3791/60068

Lyu, M., H. Suzuki, L. Kang, F. Gaspal, W. Zhou, J. Goc, L. Zhou, J. Zhou, W. Zhang, Z. Shen, et al. 2022. ILC3s select microbiota-specific regulatory T cells to establish tolerance in the gut. *Nature.* 610:744–751. https://doi.org/10.1038/s41586-022-05141-x

Martinez-Gonzalez, I., L. Mathä, C.A. Steer, M. Ghaedi, G.F. Poon, and F. Takei. 2016. Allergen-experienced group 2 innate lymphoid cells acquire memory-like properties and enhance allergic lung inflammation. *Immunity*. 45:198–208. https://doi.org/10.1016/j.immuni.2016.06.017

Melo-Gonzalez, F., and M.R. Hepworth. 2017. Functional and phenotypic heterogeneity of group 3 innate lymphoid cells. *Immunology*. 150:265–275. https://doi.org/10.1111/imm.12697

Mortha, A., A. Chudnovskiy, D. Hashimoto, M. Bogunovic, S.P. Spencer, Y. Belkaid, and M. Merad. 2014. Microbiota-dependent crosstalk between macrophages and ILC3 promotes intestinal homeostasis. *Science*. 343:1249288. https://doi.org/10.1126/science.1249288

Murray, P.J., and T.A. Wynn. 2011. Protective and pathogenic functions of macrophage subsets. *Nat. Rev. Immunol.* 11:723–737. https://doi.org/10.1038/nri3073

Paik, D., L. Yao, Y. Zhang, S. Bae, G.D. D'Agostino, M. Zhang, E. Kim, E.A. Franzosa, J. Avila-Pacheco, J.E. Bisanz, et al. 2022. Human gut bacteria produce T_H17-modulating bile acid metabolites. *Nature.* 603:907–912. https://doi.org/10.1038/s41586-022-04480-z

Pandey, A., M. Kurera, and S.M. Man. 2023. Primary intestinal fibroblasts: Isolation, cultivation, and maintenance. *Methods Mol. Biol.* 2691:327–335. https://doi.org/10.1007/978-1-0716-3331-1_23

Ricardo-Gonzalez, R.R., S.J. Van Dyken, C. Schneider, J. Lee, J.C. Nussbaum, H.E. Liang, D. Vaka, W.L. Eckalbar, A.B. Molofsky, D.J. Erle, and R.M. Locksley. 2018. Tissue signals imprint ILC2 identity with anticipatory function. *Nat. Immunol.* 19:1093–1099. https://doi.org/10.1038/s41590-018-0201-4

Saraiva, M., and A. O'Garra. 2010. The regulation of IL-10 production by immune cells. *Nat. Rev. Immunol.* 10:170–181. https://doi.org/10.1038/nri2711

Schroeder, J.H., G. Beattie, J.W. Lo, T. Zabinski, N. Powell, J.F. Neves, R.G. Jenner, and G.M. Lord. 2023. CD90 is not constitutively expressed in functional innate lymphoid cells. *Front. Immunol.* 14:1113735. https://doi.org/10.3389/fimmu.2023.1113735

Schuijs, M.J., S. Png, A.C. Richard, A. Tsyben, G. Hamm, J. Stockis, C. Garcia, S. Pinaud, A. Nicholls, X.R. Ros, et al. 2020. ILC2-driven innate immune checkpoint mechanism antagonizes NK cell antimetastatic function in the lung. *Nat. Immunol.* 21:998–1009. https://doi.org/10.1038/s41590-020-0745-y

Shouval, D.S., L. Konnikova, A.E. Griffith, S.M. Wall, A. Biswas, L. Werner, M. Nunberg, J. Kammermeier, J.A. Goettel, R. Anand, et al. 2017. Enhanced TH17 responses in patients with IL10 receptor deficiency and infantile-onset IBD. *Inflamm. Bowel Dis.* 23:1950–1961. https://doi.org/10.1097/MIB.0000000000001270

Solt, L.A., and T.P. Burris. 2012. Action of RORs and their ligands in (patho) physiology. *Trends Endocrinol. Metab.* 23:619–627. https://doi.org/10.1016/j.tem.2012.05.012

Steer, C.A., L. Matha, H. Shim, and F. Takei. 2020. Lung group 2 innate lymphoid cells are trained by endogenous IL-33 in the neonatal period. *JCI Insight*. 5:e135961. https://doi.org/10.1172/jci.insight.135961

Stockis, J., T. Yip, J. Moreno-Vicente, O. Burton, Y. Samarakoon, M.J. Schuijs, S. Raghunathan, C. Garcia, W. Luo, S.K. Whiteside, et al. 2024. Cross-talk between ILC2 and Gata3(high) T(regs) locally constrains adaptive type 2 immunity. *Sci. Immunol.* 9:eadl1903. https://doi.org/10.1126/sciimmunol.adl1903

Szeto, A.C.H., P.A. Clark, A.C.F. Ferreira, M. Heycock, E.L. Griffiths, E. Jou, J. Mannion, S.L. Luan, S. Storrar, M.D. Knolle, et al. 2024. Mef2d potentiates type-2 immune responses and allergic lung inflammation. *Science*. 384:eadl0370. https://doi.org/10.1126/science.adl0370

Tsou, A.M., H. Yano, C.N. Parkhurst, T. Mahlakõiv, C. Chu, W. Zhang, Z. He, K.J. Jarick, C. Zhong, G.G. Putzel, et al. 2022. Neuropeptide regulation of non-redundant ILC2 responses at barrier surfaces. *Nature.* 611:787–793. https://doi.org/10.1038/s41586-022-05297-6

Vivier, E., D. Artis, M. Colonna, A. Diefenbach, J.P. Di Santo, G. Eberl, S. Koyasu, R.M. Locksley, A.N.J. McKenzie, R.E. Mebius, et al. 2018. Innate lymphoid cells: 10 Years on. *Cell*. 174:1054–1066. https://doi.org/10.1016/j.cell.2018.07.017

Walker, J.A., C.J. Oliphant, A. Englezakis, Y. Yu, S. Clare, H.R. Rodewald, G. Belz, P. Liu, P.G. Fallon, and A.N. McKenzie. 2015. Bcl11b is essential for group 2 innate lymphoid cell development. *J. Exp. Med.* 212:875–882. https://doi.org/10.1084/jem.20142224

Yang, X.O., B.P. Pappu, R. Nurieva, A. Akimzhanov, H.S. Kang, Y. Chung, L. Ma, B. Shah, A.D. Panopoulos, K.S. Schluns, et al. 2008. T helper 17 lineage differentiation is programmed by orphan nuclear receptors ROR alpha and ROR gamma. *Immunity*. 28:29–39. https://doi.org/10.1016/j.immuni.2007.11.016

Supplemental material

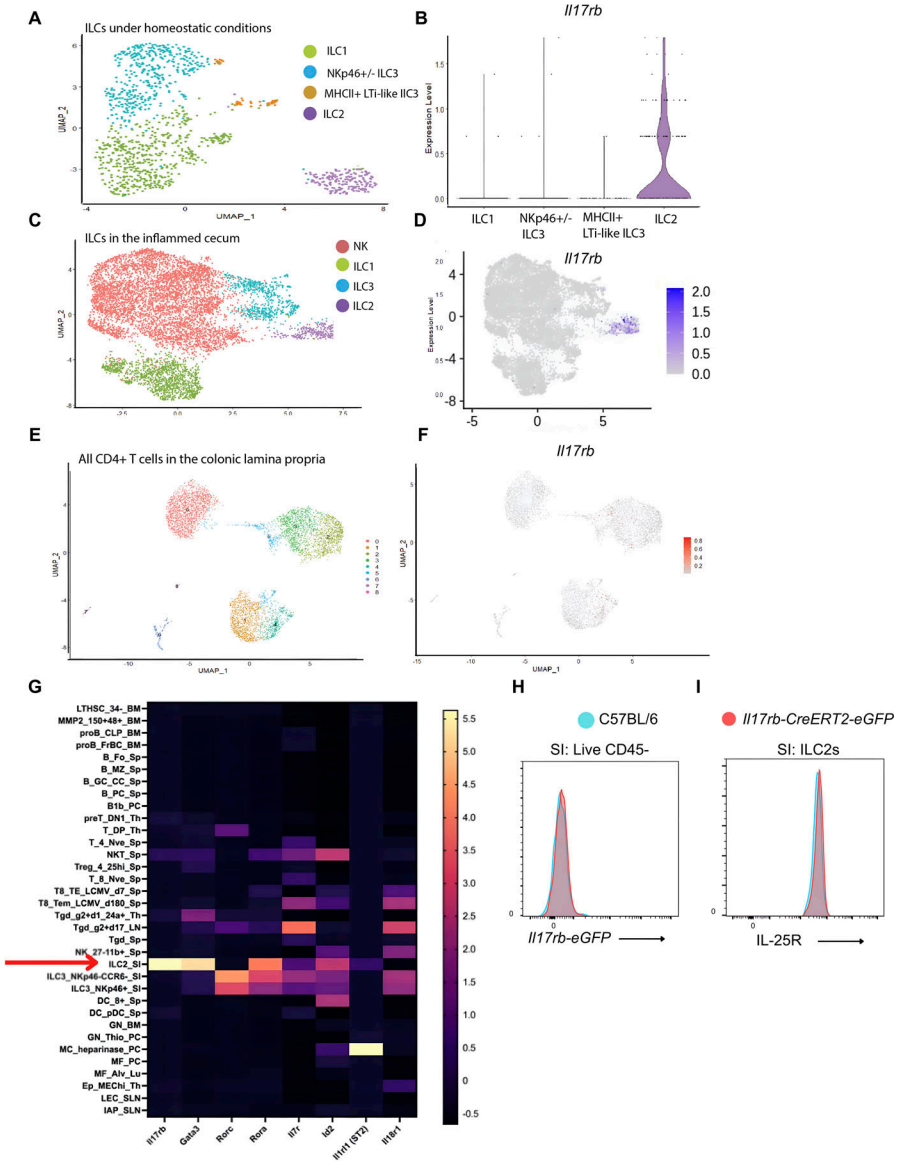

Figure S1. ***Il17rb* is uniformly expressed by tissue ILC2s. (A)** scRNA-seq of ILCs isolated from SI (reanalyzed from Gury-BenAri et al. [2016]). **(B)** Representative violin plot of *Il17rb* expression by ILCs at naïve steady-state conditions. **(C)** scRNA-seq of ILCs isolated from *Salmonella*-infected ceca (reanalyzed from Lo et al. [2019a]). **(D)** Representative violin plot of *Il17rb* expression by ILCs from inflamed ceca. **(E)** ScRNA-seq of colonic CD4+ T cells (Kiner et al., 2021). **(F)** *Il17rb* expression by CD4+ colonic T cells. **(G)** *Il17rb* expression based on the publicly accessible Immunological Genome Project (Benoist et al., 2012). **(H)** Representative histogram of eGFP expression by non-immune cells ($CD45^-$ cells) in the SI-LP. **(I)** Representative histogram of IL-25R expression by $Lineage^-IL\text{-}25R^+KLRG1^+$ ILC2s in *Il17rb-CreERT2-eGFP* and C57BL/6 mice. Data from H and I are representative of two to three independent experiments.

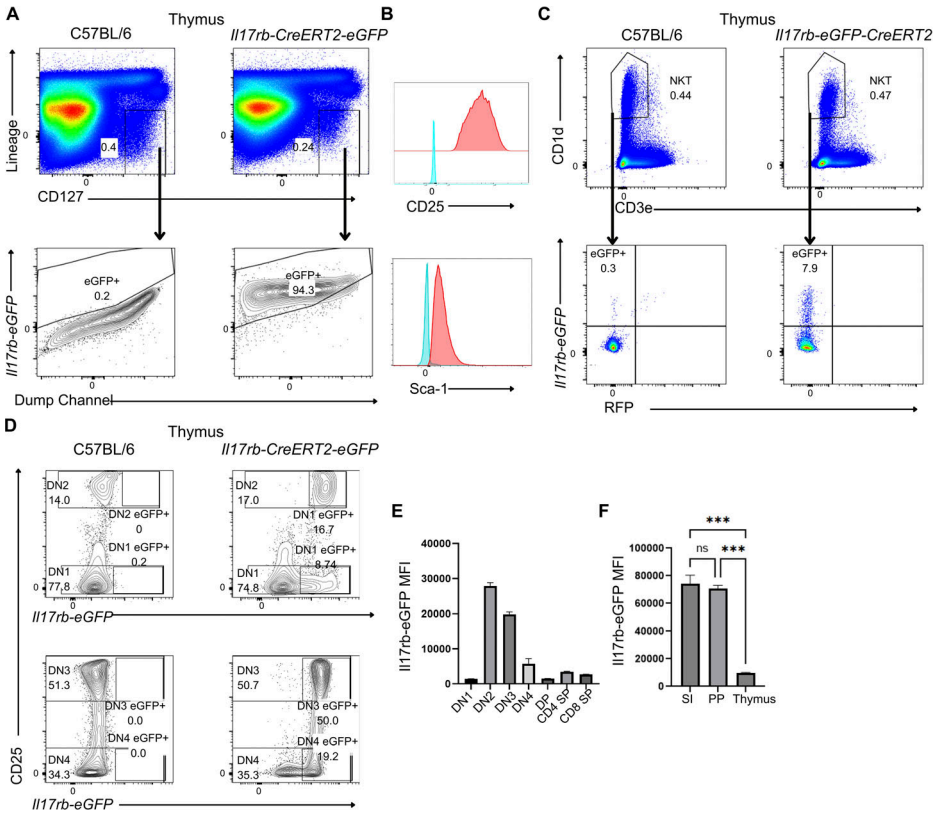

Figure S2. ***Il17rb* expression in the thymus. (A)** Representative flow cytometry plots showing *Il17rb*-eGFP expression within live CD45$^+$Lineage$^-$CD127$^+$ cells. **(B)** Representative histogram depicting CD25 and Sca-1 expression on live CD45$^+$Lineage$^-$CD127$^+$*Il17rb*$^+$ cells in the thymus. **(C)** Representative flow cytometry plots of *Il17rb* expression within CD45$^+$CD1d$^+$ NKT cells in the thymus. **(D)** Representative gating strategy for DN progenitors in the thymus (DN1 cells: CD45$^+$CD4$^-$CD8$^-$CD44$^+$CD25$^-$, DN2 cells: CD45$^+$CD4$^-$CD8$^-$CD44$^+$CD25$^+$, DN3 cells: CD45$^+$CD4$^-$CD8$^-$CD44$^{-/low}$CD25$^+$, DN4 cells: CD45$^+$CD4$^-$CD8$^-$CD44$^{-/low}$CD25$^-$). **(E)** *Il17rb* expression across DN1, DN2, DN3, and DN4 subsets (n = 3 mice). **(F)** *Il17rb* expression levels in Lineage$^-$*Il17rb*$^+$ cells isolated from the SI, PP, and thymus (n = 3 mice). Data are representative of two independent experiments and are presented as the mean ± SEM. Statistical significance in F was determined by a one-way ANOVA with Tukey's multiple comparison test (***P < 0.001; ns, not significant). PP, Peyer's patches.

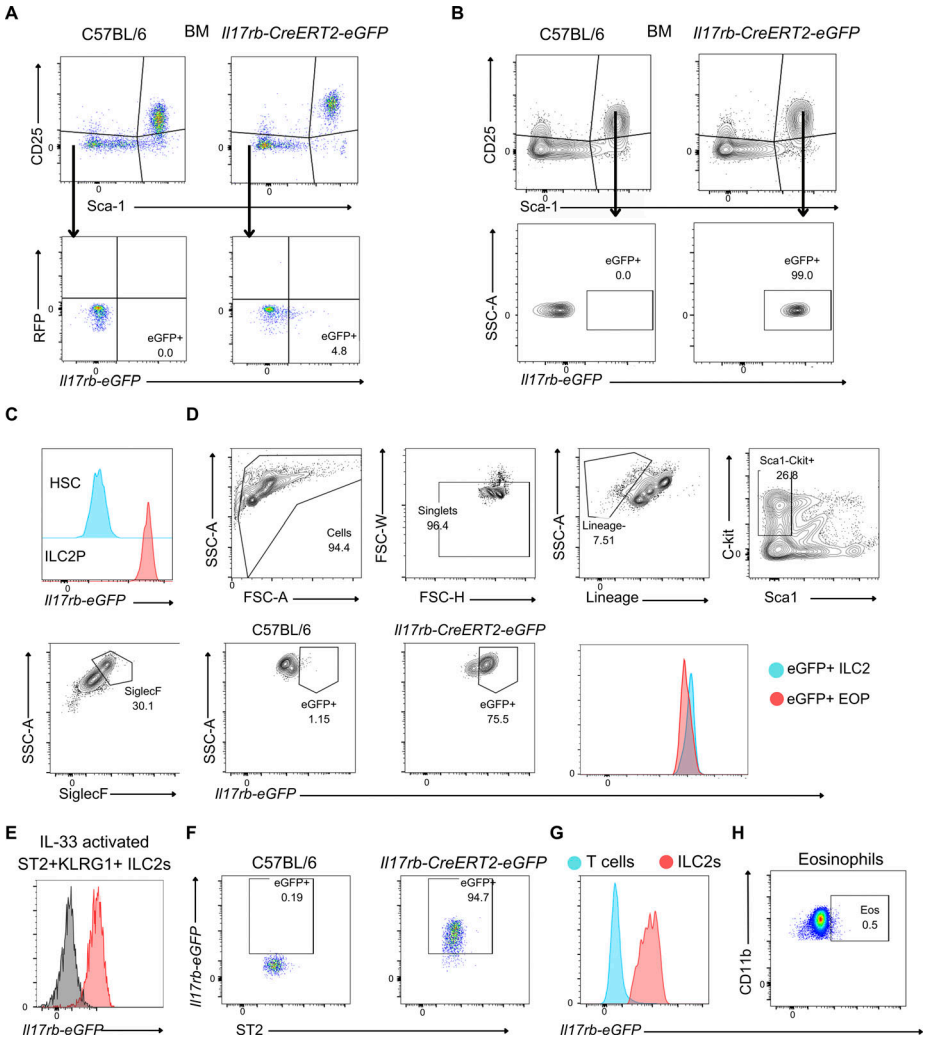

Figure S3. ***Il17rb* expression in the BM and during IL-33–induced type 2 inflammation. (A)** Representative flow cytometry plots showing *Il17rb* expression in CLPs and CHILPs (immunophenotype: CD45$^+$Lineage$^-$Sca1$^{-/int}$CD25$^-$). **(B)** Representative flow cytometry plots of *Il17rb* expression in CD45$^+$Lineage$^-$Sca1^{high}CD25$^+$ ILC2s. **(C)** Representative histogram of eGFP expression by LSK (Lineage$^-$Sca-1$^+$C-kit$^+$) versus BM ILC2s (Lineage$^-$CD127$^+$Sca-1$^+$CD25$^+$) in *Il17rb-CreERT2-eGFP* and C57BL/6 mice. **(D)** Representative flow cytometry plots showing *Il17rb* expression in eosinophil progenitors. **(E)** Representative histogram depicting *Il17rb* expression in lung ILC2s (Lineage$^-$CD127$^+$ST2$^+$KLRG1$^+$) during IL-33–induced inflammation (gray: C57BL/6; red: *Il17rb*-CreERT2-eGFP). **(F)** Representative flow cytometry plots showing *Il17rb* expression in live CD45$^+$Lineage$^-$CD127$^+$ST2$^+$ ILC2s. **(G)** Representative histogram comparing *Il17rb* expression in live CD45$^+$CD3$^+$ T cells and Lineage$^-$CD127$^+$ST2$^+$ ILC2s in the lungs. **(H)** *Il17rb* expression in CD45$^+$CD11c$^-$CD11b$^+$SiglecF$^+$ eosinophils during IL-33–induced airway inflammation. Data are representative of two to three independent experiments. CLPs, common lymphoid progenitors; CHILPs, common helper innate lymphoid progenitors.

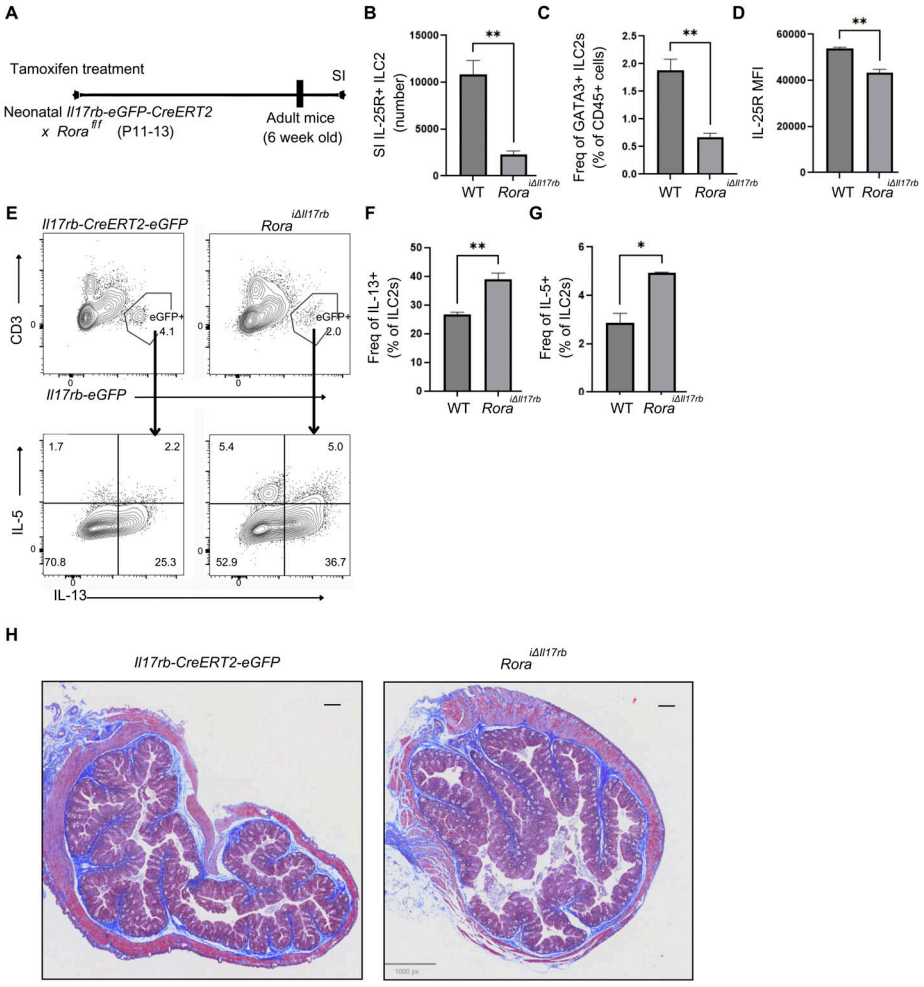

Figure S4. **RORα regulates ILC2 survival, cytokine production, and heterogeneity in the SI. (A)** Experimental schematic outlining tamoxifen treatment and analysis timeline. **(B)** Quantification of the absolute number of CD45$^+$Lineage$^-$IL-25R$^+$*Il17rb*$^+$ cells in the SI (n = 3 mice). **(C)** Quantification of the frequency of CD45$^+$CD3$^-$GATA3$^+$*Il17rb*$^+$ cells in the SI (n = 3 mice). **(D)** IL-25R expression levels in CD45$^+$Lineage$^-$IL-25R$^+$ ILC2s (n = 3 mice). **(E)** Flow cytometry plots of CD3$^-$*Il17rb*$^+$ ILC2s and their subsequent IL-5 and IL-13 production. **(F–G)** Quantification of the frequency of IL-5$^+$ and IL-13$^+$ *Il17rb*$^+$ cells among ILC2s (n = 3 mice). **(H)** Masson's trichrome staining of the cecum in naïve tamoxifen-treated *Il17rb-CreERT2-eGFP* and *Rora*^{il17rb} (*Rora*^{il17rb} refers to *Il17rb-CreERT2-eGFP* × *Rora*$^{fl/fl}$ mice). Scale bar = 100 µm. Data are representative of two independent experiments and are presented as the mean ± SEM. For intracellular cytokine detection, isolated cells were stimulated with 50 ng/ml PMA (Sigma-Aldrich) and 750 ng/ml ionomycin (Sigma-Aldrich) for 4–6 h in the presence of 10 µg/ml brefeldin A (Sigma-Aldrich) in complete RPMI-1640 medium (containing 10% FBS, 50 mM 2-mercaptoethanol, 1 mM L-glutamine, 100 U/ml penicillin, and 100 µg/ml streptomycin) to evaluate cytokine production. Statistical significance was determined using an unpaired two-tailed t test (*P < 0.05, **P < 0.01). PMA, phorbol 12-myristate 13-acetate.

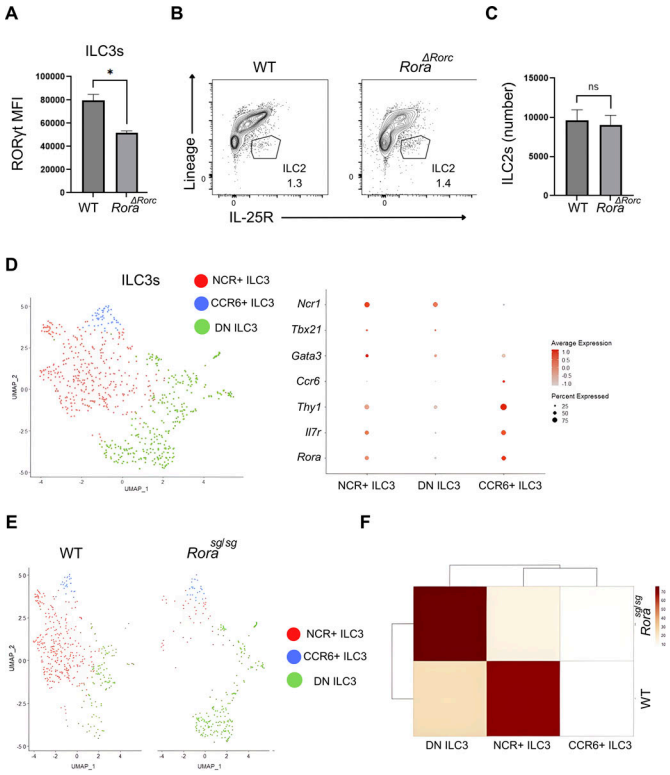

Figure S5. ***Rora* expression regulates ILC3 development and function. (A)** RORγt expression levels in Lineage$^-$CD127$^+$RORγt$^+$ ILC3s (n = 3 mice). **(B)** Representative flow cytometry plots of CD45$^+$Lineage$^-$IL-25R$^+$ ILC2s in the SI. **(C)** Quantification of ILC2 numbers in the SI (n = 4–5 mice). **(D)** UMAP of scRNA-seq of ILC3s in the cecum during intestinal fibrosis, revealing three distinct clusters: DN ILC3s, NCR$^+$ ILC3s, and CCR6$^+$ ILC3s (reanalyzed from Lo et al. [2019a]). **(E)** UMAP of scRNA-seq depicting ILC3 subsets in RORα$^{sg/sg}$ mice and control littermates. **(F)** Heatmap showing the frequency of ILC3 subsets differing between RORα$^{sg/sg}$ mice and control littermates during intestinal fibrosis. WT mice refer to *Rora*$^{fl/fl}$ littermate controls. Data from A and C are representative of two independent experiments. Statistical significance was determined using an unpaired two-tailed t test (*P < 0.05; ns, not significant).